Research Article

Harish K. Garg, Shubham Sharma*, Rajesh Kumar, Alakesh Manna, Changhe Li, Kuwar Mausam, and Elsayed Mohamed Tag Eldin*

Multi-objective parametric optimization on the EDM machining of hybrid SiC_p/Gr_p/aluminum nanocomposites using Non-dominating Sorting Genetic Algorithm (NSGA-II): Fabrication and microstructural characterizations

https://doi.org/10.1515/rams-2022-0279
received August 24, 2022; accepted November 01, 2022

Abstract: In this study, different input parameters for electric discharge machining (EDM) are examined in order to revise the distinctiveness of EDM for machining aluminum-based hybrid metal matrix composites (MMCs). The versatility of hybrid aluminum MMCs makes them very popular and sought after in the automotive, aerospace, marine, and space industries. In this article, an optimized process parameter setting for hybrid MCCs machining with an EDM machine is determined that have silicon carbide (SiC_p) and graphite (Gr_p) particles added as reinforcement materials in varying amounts (Al–0.7Fe–0.6Si–0.375Cr–0.25Zn/10 wt%SiC/3 wt%Gr–MMC, Al–0.7Fe–0.6Si–0.375Cr–0.25Zn/15 wt%SiC/5 wt%Gr–MMC, and Al–0.7Fe–0.6Si–0.373Cr–0.25Zn/20 wt%SiC/8 wt%Gr–MMC). The stir casting method was used to prepare these hybrid aluminum MMCs (3 samples). A study of surface roughness (SR) and material removal rate (MRR) was conducted to examine the effects of dominant parameters. An experiment is planned using a central composite rotatable design (CCRD) of response surface methodology (RSM). It is possible to predict MRR and SR with 95% degree of accuracy by utilizing the quadratic model. Non-dominating Sorting Genetic Algorithm-II was employed to solve "mathematical models" for multi-objective optimization of output response characteristics. The scanning electron microscope (SEM) images of the tool and workpiece materials show that the recast layer has been formed on the tool face and the surface of the machined work-piece. Based on the results, it was determined that an optimal value of MRR (2.97 $g{\cdot}min^{-1}$) was obtained at 90 µs, 30 µs, 7.0 V, and 14 A as P_{on}, P_{off}, gap voltage, and peak current, respectively. As a result of the findings, the SR is reciprocally proportional to P_{on}, and the SR is commensurate with P_{off}. It was determined that the optimal value of SR (2.41 µm) could be attained at 30 µs, 52 µs, 6.0 V, and 12 A as the P_{on}, P_{off}, gap voltage, and peak current, respectively. For an optimal set of response variables, P_{on} can be specified as 30 µs, P_{off} as 30 µs, gap voltage as 6 V, and peak current as 14 A as process parameters for MRR and SR. The SEM images of the tool material and the workpiece material clearly demonstrate a recast layer formed on the tool face and the machined surface of the workpiece. The optical microscopy analysis reveals a uniform distribution of SiC_p and

* **Corresponding author: Shubham Sharma,** Department of Mechanical Engineering, University Centre for Research and Development and Chandigarh University, 140413, Punjab, India; School of Mechanical and Automotive Engineering, Qingdao University of Technology, 266520, Qingdao, China, e-mail: shubham543sharma@gmail.com, shubhamsharmacsirclri@gmail.com
* **Corresponding author: Elsayed Mohamed Tag Eldin,** Faculty of Engineering and Technology, Future University in Egypt, New Cairo 11835, Egypt, e-mail: elsayed.tageldin@fue.edu.eg
Harish K. Garg: Department of Mechanical Engineering, DAV University, Jalandhar, Punjab, 144012, India, e-mail: harish10026@davuniversity.org
Rajesh Kumar: Department of Mechanical Engineering, Sant Longowal Institute of Technology, Longowal, Punjab, 148-106, India, e-mail: rajesh_krs@rediffmail.com
Alakesh Manna: Department of Mechanical Engineering, PEC University of Technology, Chandigarh, 160-012, India, e-mail: kgpmanna@gmail.com
Changhe Li: School of Mechanical and Automotive Engineering, Qingdao University of Technology, 266520, Qingdao, China, e-mail: sy_lichanghe@163.com
Kuwar Mausam: Department of Mechanical Engineering, GLA University, Mathura, UP, 281406, India, e-mail: Kuwar.mausam@gla.ac.in

Gr_p particles in the Al–0.7Fe–0.6Si–0.375Cr–0.25Zn matrix. In addition to recast layers and machined surfaces, EDS analysis reveals the deposition of tool material on the surface of the workpiece. The composites fabricated may replace materials in many of these applications where "friction" is a significant factor.

Keywords: electric discharge machining, hybrid MMC, MRR, multi-response optimization, CCRD, RSM, SR, morphology

Nomenclature

ANOVA	analysis of variance
CCRD	central composite rotatable design
CLA	centerline average
EDM	electric discharge machining
EDS	energy dispersive X-ray spectrometer
GRA	gray relational analysis
Gr_p	graphite particles
MMC	metal matrix composite
MRR	material removal rate
NSGA-II	Non-dominating Sorting Genetic Algorithm-II
PC	powder concentration
RSM	response surface methodology
RLT	recast layer thickness
SEM	scanning electron microscopy
SiC_p	silicon carbide particles
SI	surface integrity
SMA	shape memory alloys
SON	spark on duration
SOFF	spark off duration
SR	surface roughness
T_{off}	pulse off time

1 Introduction

In order to prevent degradation of the material characteristics during machining, "precision machining" is challenging because both soft-matrix phase and hard-reinforced particles are present. The advent of computers in manufacturing and production technology led to a radical change in the 1980s when traditional machines were almost replaced with computer numerical control machines, such as electric discharge machining (EDM) [1–3]. For tasks such as machining electrically conductive work material, EDM is used as it is highly accurate and can be used for complex geometries with high productivity. For advanced work materials, EDM is used on a wide-reaching scale. The price and quality standard of the final manufactured goods play an essential job in the existence and survival of modern manufacturing factories. Control parameters of EDM play a decisive role in selecting the product price and quality standard of manufacturing. Hybrid aluminum metal matrix composites (MMCs), because of their wide applications in the automobile and space industry, are in high demand and possess unique tailorable properties such as lightweight, high durability, good resistance to wear, and a low coefficient of thermal expansion [4]. Because of the possession of superior stiffness and reinforcement strength, hybrid composite materials are hard to process through conventional methods [3–6]. In this regard, the EDM process becomes an effective method for these kinds of composite materials [5–8]. EDM is the way towards machining electrically conductive materials through the means of precisely controlled sparks that occur between an electrode and a workpiece when the dielectric liquid is present. The dielectric fluid works as an electrical encasing unless adequate voltage is applied to bring it to its ionization position when it turns into a good conductor of electricity or heat [9–13]. The subsequent spark discharge erodes the work part or job to shape into a required contour. Among the variety of fabrication processes available, stir casting is generally accepted because of its simplicity, flexibility, and low cost. Bodunrin et al. [6] cited the significant demand for Al hybrid MMC in engineering applications as a result of the superior mechanical and tribological properties of these materials. To further improve the performance of hybrid MMC, the right reinforcements need to be added into an ethical composition [6,14–17]. Kansal et al. [7] fabricated a hybrid MMC at a modest cost with a strong performance index. Because of its wide range of applications, hybrid MMC is used in a variety of industries [7,18–21]. The performance of the hybrid MMC has been observed to be low due to the poor mixture of armatures and matrix alloy. Authors concluded that the reliability and flexibility rates are very much high for hybrid MMC. James et al. [8] analyzed the effect of SiC and TiB_2 as particulates to produce hybrid-MMC. Increasing the weight percentage of SiC and TiB_2 had legitimate effects on the mechanical and tribological properties, according to the results [8,22–24]. Analysis of variance demonstrated the reinforcing of TiB_2 unswervingly influenced the recitals and surface quality characteristics. Chaudhary and Jadoun [9] revealed that EDM is a suitable non-traditional method to accomplish the superlative positioning. EDM process is utilized to shape the rigid metallic materials and to create a profound multifaceted intricate shape [25–27]. In the past few years, numerous investigators have done entire forms of EDM for their tentative experimentation trials because of their higher and advanced superior applications. Sarkar

et al. [10] conducted a superlative optimum machining factors of EDM at which the surface roughness (SR) attains a lesser valued level, while the material removal rate (MRR) reaches a higher valued level. In a study of the recital performance, four operating procedural factors were varied up to three stages, and MRR and SR were measured [28–30]. The L_{27} orthogonal array has been utilized to progress an ultimate experimentation trial design. A repeated test at particular set of machining parameters was carried out to confirm the output. Kumar et al. [11] determined the feasible variables of EDM of a microwave thermal processed, aluminum graded hybrid MMC. Thermally processed aluminum-boron carbide (15 vol%) and Plumbago (5 vol%) were stirred up via liquid state processing method to prepare a hybrid aluminum MMC. Through trial investigational analysis, they revealed an utmost persuasive machining factor for required manufacture [31–33]. Beri et al. [12] examined the ANOVA and signal to noise ratio techniques to find out the influence of input parameters of EDM for attaining a required performance (MRR and tool wear rate (TWR)) for an Al 2618 based hybrid MMC. Pulse-on time and current showed their significant effects on MRR and TWR. Ghosal et al. [13] examined the consequences of diverse factors throughout the machined processing of aluminum/Al_2O_3-MMC by Ytterbium fiber lasers. The precise scientific model was produced for accomplishing superior machining operation. Response surface methodology (RSM) was selected to mainly recognize momentous substantial factors for achieving the optimal response. Garg et al. [14] employed the RSM approach for designing the final experiment matrix. From the literature review, it is evident that a lot of work has been carried out in the characterization of aluminum-based composites. However, a little work has been reported on the machining characteristics of aluminum-based hybrid composites [34–36]. An investigation was undertaken by Kenneth Kanayo Alaneme for "aluminum matrix hybrid composites" reinforced with Al_2O_3, rice husk ash (RHA), and Gr in order to determine their microstructural characteristics, mechanical characteristics, and wear behavior [37]. Bisaria and Shandilya [38] demonstrated that surface crack density is directly correlated with pulse on time, while micro-hardness is directly correlated with spark gap voltage and pulse on time, but inversely correlated with spark gap voltage and pulse off time. Using silicon carbide as reinforcement, Arora and Sharma [39] found that composites increased in density by 1.8%, hardness by 37%, and tensile strength by 39%, despite a decrease in density of 3.9%. For composites reinforced with RHA, hardness and tensile strength were improved by 16 and 21%, respectively. As a result of adding 5 wt% SiC to conventional sintering (CS) and electric resistance sintering (ERS), Shaikh et al. [40] demonstrated that hardness improved in the CS batch by 32% and wear resistance increased in the ERS batch by 40%, while coefficient of friction improved in the CS and ERS batch by 32 and 62%, respectively. In the powder-mixed electrical discharge machining (PM-EDM) process, research was primarily concerned on improving the output results, which include MRR, TWR, and SR as reported by the Alhodaib et al. [41]. The other key output responses, such as recast layer thickness, overcut, and microhardness, have not received much attention. Only a few studies have been reported on PM-EDM of Nimonic-90. A PM-EDM setup is used to machine Nimonic-90 using silicon powder mixed with kerosene after considering previous arguments. In the work explored by Alhodaib et al., the aim is to determine the impact of dominant process parameters such as the powder concentration (PC), discharge current (IP), spark on duration (SON), and spark off duration (SOFF) on the amount of SR, and the thickness of the recast layer (RLT) [41]. Multi-response optimization was performed using gray relational analysis (GRA) in order to determine the minimum RLT and SR. When silicon powder is added to kerosene oil, the SR of the recast layer is significantly reduced as compared to the thickness of the recast layer when using kerosene oil alone. Both the SR and thickness of the recast layer were significantly influenced by SON. A GRA was employed to determine the minimum SR (3.107 μm) and the thinnest recast layer (14.926 μm) at optimum process parameters, including PC = 12 $g{\cdot}L^{-1}$, IP = 3 A, SON = 35 μs, and SOFF = 49 μs [41]. Because of their inherent characteristics, such as shape memory effect and super elasticity, the NiTi shape memory alloys (SMAs) find extensive applications in the aerospace, biomedical, automobile, and robotics fields [42]. In spite of these difficulties, it is difficult to machine these alloys according to conventional machining practices. This is because they exhibit numerous shortcomings, such as strain hardening, tool failure, long machining times, and poor surface quality. As a result of these challenges, performance characteristics of NiTi SMAs need to be improved. Bisaria and Shandilya have explored a variety of advanced and unconventional machining processes in recent years [42]. Among the various advanced machining processes available to machine these hard-to-machine alloys, wire electric discharge machining (WEDM) has proven to be particularly effective and a reasonable alternative. An overview of NiTi SMAs, their characteristics, applications, and conventional machining techniques have been included in this study [42]. It provides comprehensive insights into the various aspects of surface integrity (SI) for NiTi SMAs manufactured by WEDM. Specifically, the Bisaria

and Shandilya have examined the literature on SI aspects of NiTi-based SMAs, namely, surface characteristics, recast layer, phase analysis, elemental composition, microhardness, shape recovery abilities, and residual stress, which have been accomplished thus far in the domains [42]. In addition to its outstanding properties, Nimonic C-263 superalloy exhibits high-temperature resistance, high specific strength, high thermal fatigue resistance, and high corrosion resistance under heavy loads [43]. A major focus of the study by Bisaria and Shandilya have determined that how the one-parameter-at-a-time approach has affected the SR, average cutting rate, and SI of Nimonic C-263 superalloy by examining the effects of WEDM process parameters [43]. As the "spark energy," and "peak current" increased, the "SR", and "average cutting rate" also increased, while the "spark frequency" decreased [43]. In addition to "surface topography," and "morphology," Bisaria and Shandilya have also examined the RLT, elemental composition, and phase analysis of Nimonic C-263. On the micrograph of the machined surface, taken with a scanning electron microscope (SEM), discharge craters, micro-globules, and droplets of molten material can be observed on the machined surface [43]. In comparison to higher spark energies, a recast layer of minimum thickness has been formed at lower spark energies, with less transfer of foreign atoms (Mo, C, and O) [43]. As a result of XRD analysis, various Ni, Fe, Al, and Ti compounds were identified on the machined surface, including Fe1.2Ni0.8, Fe1.5Ni0.5, Co0.06Fe0.94, and Alo.29Ni0.27Ti0.44 [43]. It has therefore been attempted in the present study to develop Al-based hybrid composites with SiC, and graphite particles (Gr_p) as reinforcements. After the fabrication of composites, the composites have been evaluated for morphological, elemental mapping analysis, microstructural examination processed with different tool materials on EDM. The influence of diverse tool materials and operating input variables is investigated on the surface characteristics of hybrid composites. Thus, in this experimental work, three different Al–0.7Fe–0.6-Si–0.375Cr–0.25Zn–MMC materials were fabricated by adding the reinforcements (SiC_p and Gr_p) in three different compositions (Al–0.7Fe–0.6Si–0.375Cr–0.25Zn/10 wt%SiC/3 wt% Gr–MMC; Al–0.7Fe–0.6Si–0.37 5Cr–0.25Zn/15 wt%SiC/ 5 wt%Gr–MMC, and Al–0.7Fe–0.6Si–0.375Cr–0.25Zn/20 wt % SiC/8wt %Gr–MMC). The electric discharge machine has a number of machining parameters, but in this study, six significant operating factors (P_{on}, P_{off}, current, voltage, tool, and workpiece material) were considered for the final investigation. Analyses of the SR and MRR have been conducted at varying values of the six process parameters. A final experimental plan was developed utilizing the design expert software 7.0.0.

2 Experimentation: materials and methods

2.1 Fabrication of aluminum-based hybrid MMCs

The aluminum alloy Al6061 as a base matrix is electrically charged in a graphite container (crucible) and heated to nearly 750°C until the whole metal in the container has been liquefied [15,44,45]. Melting temperature of Al6061 is 650°C, which is quite less than the set temperature of the muffle furnace. This temperature difference helps in melting the aluminum alloy at a faster rate and reduces the oxidation level. It also improves the wettability of the reinforced particles in the base matrix [16,46,47]. In this experimental work, three different aluminum-based hybrid composite materials have been fabricated by varying weight percentages of reinforcements (SiCp and Grp) of 200 mesh size (average size of 75 μm) as reinforcements. It was discovered that cubic boron nitride cutting tools could not be used to machine MMC containing SiC particles of 110 μm because the cutting edge and nose were heavily fractured [17,48,49]. SiCp and Grp have been preheated separately at 630°C for 3 h in another electric muffle furnace [50–52]. By doing so, the absorbed hydroxide and other gases are removed from the reinforcements. The temperature of retort kiln based electrical furnace was initially maintained at a temperature beyond the melting temperature of Al alloy, i.e., at 750°C to completely liquefy the Al compound and after that it is cooled down to 630°C to transform it to semi-solid state. Preheated particles of SiC and graphite in three different weight percentage as shown in Table 1 have been poured (one by one) into semi solid aluminum alloy. To enhance the wettability of the reinforcements and prevent particles from setting at the bottom of the crucible, a stirrer made of graphite was lowered gently into the melt and speeded up to 500 rpm to stir the molten metal [53–55]. The rotation speed of the stirrer can be controlled employing a regulator provided on the stirrer [56–58]. Magnesium powder as a wetting agent was added by 1% by weight to increase the wettability [20–38].

Table 1: Composition merits for three different Al MMCs

Hybrid composite	Reinforcements	
	SiC_p (%)	Gr_p (%)
Workpiece 1: Al MMC-1	10	3
Workpiece 2: Al MMC-2	15	5
Workpiece 3: Al MMC-3	20	8

The mixture was then reheated to a temperature of 750°C to change the composite to a complete liquid state and then the composite was immediately poured to a preheated metallic mold. To obtain uniform solidification, the mixture was also heated to 500°C for 30 min in the mold [59–61]. It was assured that the composite poured in the mold was in the liquid state all through the pouring time. This mixture in the metal mold was kept at ambient room temperature to acquire solidification [62–64]. From the existing studies, it has been unveiled to merge reinforcement particulates with Al molten matrix at a volume fraction of 30% [65,66]. It has been found that weight fractions of SiC, graphite, and alumina (5, 10, 15, 20, 25, and 30%) varied significantly, whereas graphite weight fractions of 2, 4, 6, 8, and 10% and all other components kept constant. It has been observed from the results of this study that hardness increases with an increase in the composition of SiC. In this study, the most promising results were obtained with a weight fraction of 25% for SiC particles. A maximum hardness of 45.5 BHN can be achieved. The stirring process results in a more homogeneous dispersion of SiC particles in the Al matrix. When graphite particles are added to the matrix with a strong interfacial bond, the particle distribution and mechanical properties of the composites are significantly improved. Graphite particles with a 4% weight fraction produced the most favorable results. It has been reported that the maximum hardness is 74 BHN. Compared to SiC reinforcement, Al reinforced with graphite showed higher interfacial binding and higher mechanical properties [37–39,66,67]. In order to develop the monolithic composites of AA-6351/SiC and "AA-6351/RHA," the stir casting technique was employed [39]. As specified, AA-6351 ingots were melted in a graphite crucible in a temperature range of 830–860°C using an electric furnace [39]. To develop the composites, the determined quantities of SiC and RHA (2, 4, 6, and 8 wt%) were preheated at 520 and 270°C, respectively. A 400 rpm stirring was performed for 10–12 min in order to ensure uniform distribution of the reinforcement in the melting matrix. After the composites had been fabricated, they were cooled and then collected from the crucible [39]. Thus, in this study, the experimental investigation has been carried out by taking 28% of reinforcing constituents of SiC_p and Gr_p within Al matrix composites using stir casting for automobile, aviation, and electronics sectors.

2.2 Testing of prepared samples

Each aluminum-based hybrid MMC sample has been individually scanned for microstructure and homogeneity using scanning electron microscopy (SEM). Figure 1 shows a sample of Al6061 aluminum alloy with its matrix phase reinforced with SiC_p and graphite. By utilizing SEM, the uniformity of the reinforcement particles has been examined [29–43,55–67]. EDM was used to machine samples with the most uniform and thorough distribution. An energy dispersive X-ray spectrometer (EDS) was also be used to obtain qualitative, and quantitative chemical analysis information of the fabricated composite samples, as illustrated in Figure 2. Optical microscopy was completed with an optical magnifying instrument, which utilized visible light and an arrangement of focal point lenses to amplify pictures of small specimens as illustrated in Figure 3. To check the homogeneity of the prepared samples, SEM and optical microscopy have been used to examine the casted composites. After the specimens were prepared, an optical microscope- Nikon model "EPIPHOT," was used to observe the fabricated composite samples at various magnification scales. The microstructure of the casted composite is helpful to examine and ensure whether the reinforcement added to

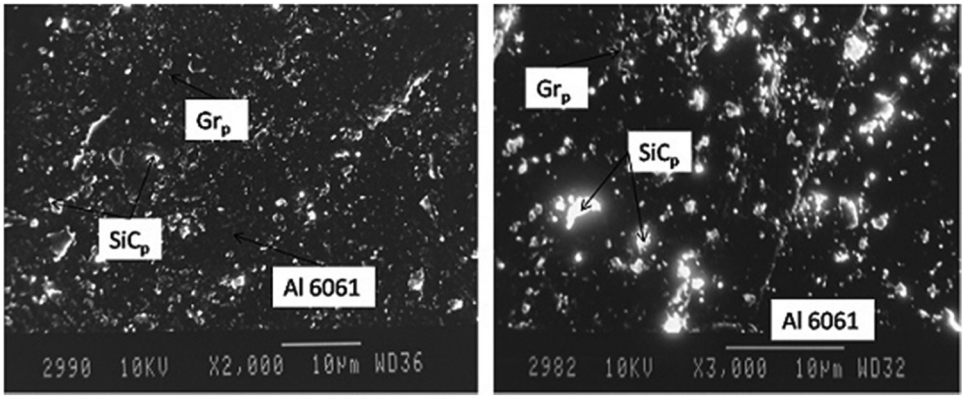

Figure 1: SEM images of Al/10 wt%SiC/3 wt%Gr–MMC hybrid composite before machining.

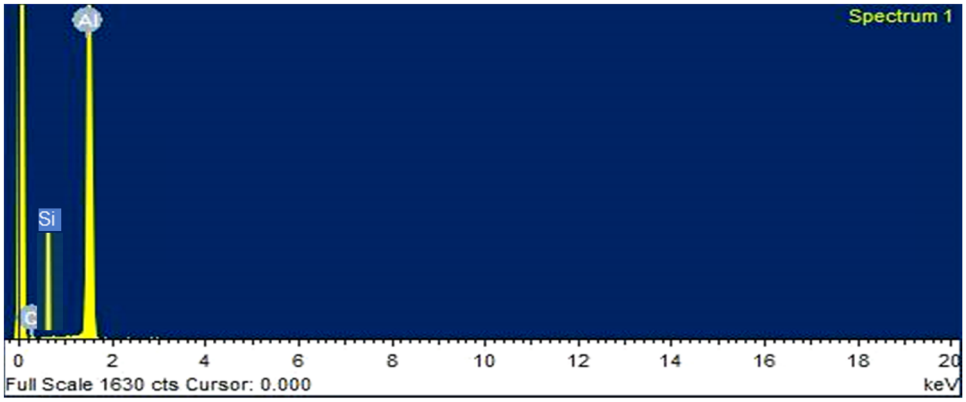

Element	Line-type	Weight%	Atomic%
C	K Series	6.32	34.34
O	K Series	5.00	08.24
Al	K Series	79.68	45.41
Si	K Series	9.00	12.01
Total		100.00	100.00

Figure 2: EDS analysis of SiC_p/Gr_p/Al-MMC hybrid composites.

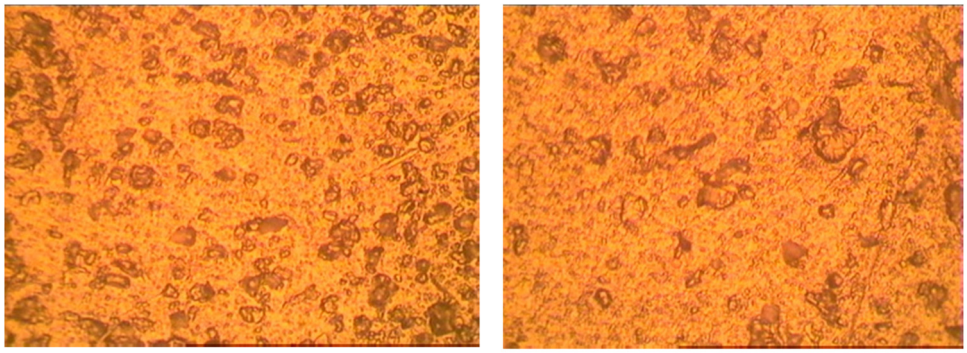

Figure 3: (a) Optical micrograph of Al-6061/15SiC/5Gr at 200× magnification and (b) optical micrograph of Al-6061/15SiC/5Gr at 400× magnification.

the base matrix is uniformly dispersed. To check the microstructure of the Al/10 wt% SiC/3 wt%Gr–MMC, a SEM by JEOL, JSM-6100, Japan placed at NITTTR, Chandigarh, has been used. A cylindrical specimen of diameter 30 mm was prepared by polishing the material from both sides followed by cleaning the specimen with acetone. EDS analysis, Oxford Instruments X-act with conventional cathode, measured the intensity of the emitted X-ray as a function of their energy. EDS figure shows the composition of reinforcements and SEM shows the uniform distribution of SiC_p and Gr_p in the base matrix [65–67]. Table 2 shows various process parameters and their levels.

3 Experimental work

The design expert software version 7.0.0 has been utilized for the design of final 52 experiments developed by the RSM approach [68–70]. These 52 experiments display various combinations of process parameters. At each combination performances or response (SR) have been checked, to improve the quality and productivity. To investigate and calculate our desired performance, experimental work on EDM has been done by varying its six process parameters up to their three levels. Table 2 shows the projected machining operating factors and their respective level. A

Table 2: Process parameters and their levels

Machining parameters	Symbols	Units	Levels		
			Level 1	Level 2	Level 3
P_{on}	T_{on}	µs	30	60	90
P_{off}	T_{off}	µs	30	60	90
Voltage	*V*	V	6	7	8
Current	*A*	Amp	10	12	14
Tool	*T*	—	Steel 304 (−1)	Brass (0)	Copper (1)
Workpiece	*w/p*	—	Al MMC (−1)	Al MMC (0)	Al MMC (1)

CMAX S645 EDM machine (Taiwan made) placed at Central Institute of Hand Tools (CIHT), Jalandhar as shown in Figure 4 has been used for this experimental work.

The EDM oil (specific gravity – 0.763) has been used as the dielectric fluid in this experimental procedure. The fabricated specimens of hybrid aluminum MMC (Al6061 + 10%SiC_p + 3%Gr), (Al6061 + 15%SiC_p + 5%Gr) and (Al6061 + 20%SiC_p + 8 Gr%) have been used as workpieces and copper, brass, and steel 304 rods of 12 mm (Ø) have been used as electrodes. EDM machine has various numbers of process parameters which directly affect its performance [71–73]. In this work, four parametric factors like P_{on}, P_{off}, voltage, and current up to three levels have been selected and their response regarding MRR and SR have been calculated. 52 experiments by RSM approach were designed for final experimental investigation as shown in Table 3, and during each experiment, a blind hole cavity of 12 mm (Ø) diameter and 1 mm depth were made. The machining time was calculated for each trial.

4 RSM

RSM is a dynamic and foremost important tool, within a specified range of the factors, it is developed to find the optimal response [74–76]. It comprises a bundle of mathematical and arithmetical techniques utilized for the competent functional association between a response variable (*y*) and several affiliated control variables expressed by x_1, x_2,., x_k [20,77–79]. For fitting a second-degree prediction equation for the output, these designs are fully capable. The objective of quality improvement can often be accomplished directly through RSM. If a maximum or minimum output response exists inside the factor limits, RSM is capable to estimate it. There are small number of factors associated as far as industrial applications are concerned.

Figure 4: The schematic outlook of an EDM.

Table 3: Design matrix and trial results for MRR and SR

Trial runs	Pulse on time (T_{on} in μs)	Pulse off time (T_{off} in μs)	Voltage (V)	Current (I)	Tool	Workpiece	SR (R_a in μm)	MRR (g·min^{-1})
1	60	60	7	12	0	0	2.74	0.862
2	60	60	7	12	0	0	2.68	0.849
3	60	60	7	12	0	0	2.74	0.86
4	60	60	7	12	0	−1.56508	3.56	1.079
5	60	60	5.43492	12	0	0	3.03	0.953
6	90	30	6	10	1	−1	4.59	2.34
7	90	90	6	10	−1	−1	4.2	1.17
8	60	60	7	8.86983	0	0	3.3502	0.704
9	30	90	8	10	−1	−1	3.822	0.48
10	60	13.0475	7	12	0	0	3.12	2.17
11	90	30	8	10	1	1	5.1858	2.12
12	60	60	7	12	0	0	2.7	0.856
13	30	30	6	14	1	−1	3.6016	2.354
14	90	30	8	14	1	−1	5.32	2.96
15	60	60	7	12	0	0	2.65	0.847
16	90	90	6	14	−1	1	4.908	1.77
17	30	90	6	14	1	1	4.1832	1.33
18	60	60	7	12	1.56508	0	4.24	1.44
19	60	60	8.56508	12	0	0	3.4512	0.879
20	30	90	8	14	1	−1	3.91	1.25
21	60	60	7	12	0	0	2.71	0.87
22	30	90	8	10	1	1	4.4	0.535
23	60	60	7	15.1302	0	0	3.6	1.94
24	30	90	6	10	−1	1	4.36	0.49
25	90	90	8	10	1	−1	4.5398	1.23
26	30	90	8	14	−1	1	4.3446	1.35
27	90	30	6	14	−1	−1	4.934	2.832
28	90	30	8	10	−1	−1	4.9746	1.94
29	90	30	6	10	−1	1	4.7684	2.103
30	60	60	7	12	0	0	2.675	0.854
31	90	90	6	14	1	−1	4.503	1.78
32	30	30	8	14	−1	−1	4.0568	2.012
33	30	30	8	10	1	−1	3.99	1.24
34	13.0475	60	7	12	0	0	2.44	0.37
35	60	60	7	12	−1.56508	0	4.3084	1.25
36	90	90	8	10	−1	1	4.55	1.222
37	60	60	7	12	0	1.56508	4.0368	1.16
38	30	90	6	10	1	−1	3.65	0.42
39	60	60	7	12	0	0	2.61	0.865
40	30	30	8	14	1	1	4.19	2.26
41	90	90	6	10	1	1	4.51	1.24
42	30	90	6	14	−1	−1	4.01	1.108
43	90	90	8	14	−1	−1	4.9258	1.72
44	106.953	60	7	12	0	0	3.69	1.5
45	90	30	8	14	−1	1	5.3768	2.73
46	30	30	6	10	−1	−1	3.78	1.26
47	90	90	8	14	1	1	5.208	2
48	30	30	6	14	−1	1	3.9362	2.21
49	30	30	8	10	−1	1	4.14	1.037
50	30	30	6	10	1	1	4.21	1.34
51	90	30	6	14	1	1	4.7756	3.11
52	60	106.953	7	12	0	0	2.92	0.714

Several factors have a direct relationship with several runs. A regression expression is constructed using experimental data. The line of the best fit based mathematical model was represented as

$$Y = f(T_{on}, T_{off}, v, c, t, w/p) + \varepsilon, \quad (1)$$

where Y is the preferred output and f is the response function. ε represents random experimental error assumed to have a zero mean value associated with the experiments, respectively. The surface generated by $f(T_{on}, T_{off}, v, c, t, w/p) + \varepsilon$ is called response surface.

$$y = \beta_0 + \sum_{i=1}^{n_d} \beta_i x_i + \sum_{i=1}^{n_d} \sum_{j \geq i}^{n_d} \beta_{ij} x_i x_j. \quad (2)$$

where x_i is the design attribute, n_d is the number of intended design attributes, β_i is the unknown coefficient, and x refers to the design matrix of experimental points.

Figures 5–7 show the recast layer formed on the workpiece. Because of the long spark gap, the eroded material gets cluster in the machining zone and stick over the surface. Recast formed on the surface is a result of high-intensity current for a long pulse on time and long gap voltage.

Figure 8 shows the analysis of the EDX of machined surfaces and recast layers on workpiece surfaces.

5 Results and discussion

To identify the main parameters (significant), in addition to the interaction effect of operating factors, and to analyze the acquired data is important. Design expert 7.0.0 ® software has been employed to ensure the competence and capability of the mathematical model. Analysis of variance technique is constructed to ensure the competence and capability of the mathematical model, lack of fit, and model summary statistics [80–82]. Multi-objective optimization is done via NSGA-II. The MRR and SR based prediction models developed by employing RSM depend upon a central composite rotatable design technique. The results obtained after the measurement of MRR and SR as shown in Tables 4 and 5 are input to Design expert 7.0.0 ® software for further analysis.

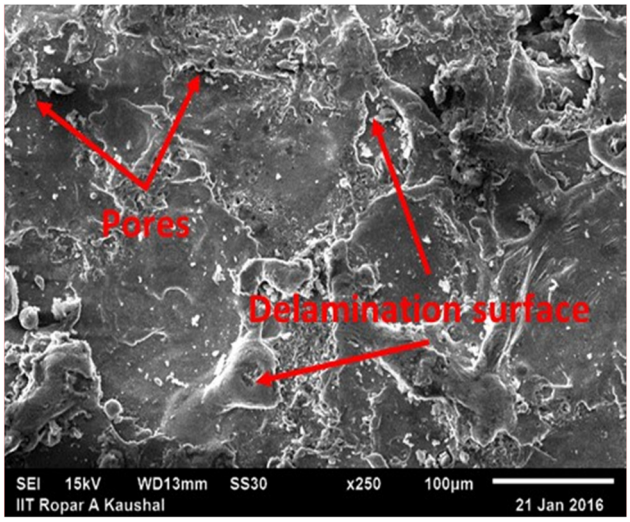

Figure 6: SEM image of Al/15 wt%SiC/5 wt%Gr–MMC hybrid composite after machining.

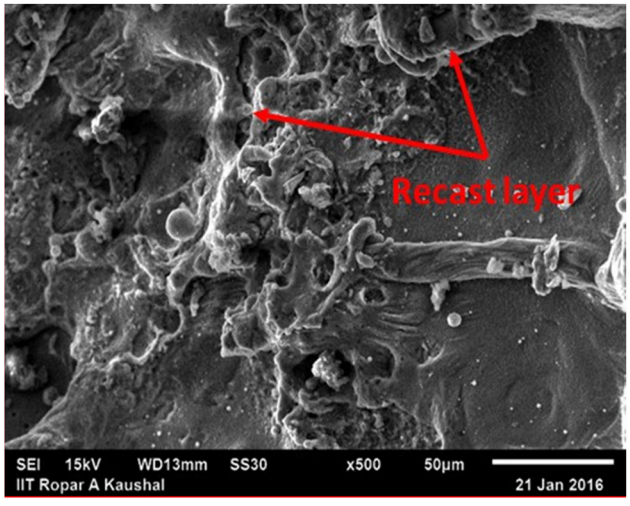

Figure 5: SEM image of Al/10 wt%SiC/3 wt%Gr–MMC hybrid composite after machining.

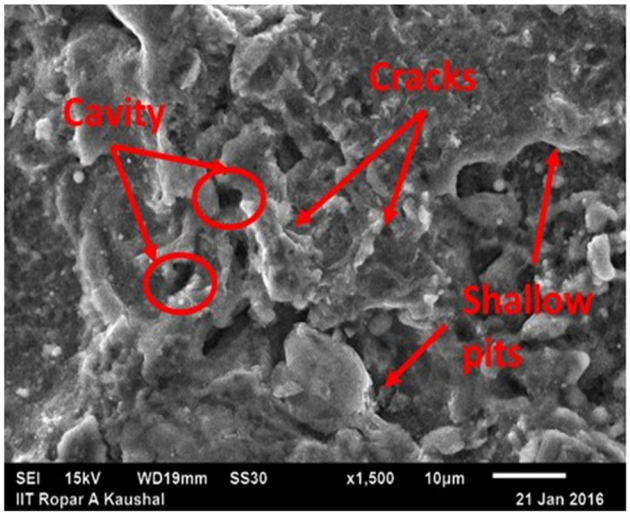

Figure 7: SEM image of Al/20 wt%SiC/8 wt%Gr–MMC hybrid composite after machining.

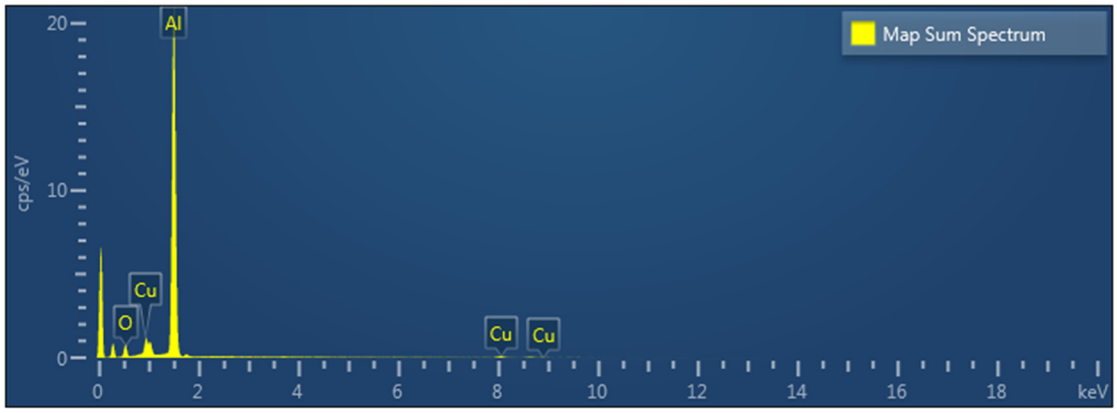

Map Sum Spectrum Element	Line Type	Weight %	Weight % Sigma	Atomic %
Al	K series	56.01	0.58	42.86
C	K series	25.43	0.67	43.71
O	K series	7.70	0.28	9.94
Cu	L series	6.27	0.28	2.04
Zn	L series	4.59	0.24	1.45
Total		100.00		100.00

Figure 8: EDX analysis of machined surface.

5.1 Analysis of MRR

Table 4 demonstrates the analysis of variance for MRR quadratic model. This investigation was carried out for significance level of $\alpha = 0.05$, i.e., for a certainty dimension-based confidence level of 95%. The estimation of "Prob. > *F*" for the model is $0.0001 \ll 0.05$, signifies that the model is considerably noteworthy, i.e., the stipulations and factors in the model significantly affect the reaction.

The insignificant model terms can be removed to obtain an improved model. Lack of fit *F* value of 3.362677 entails that the lack of fit was not noteworthy comparative or relative to the pure error. There is a 0.906056963% probability to facilitate a lack of fit *F* value and this large could occur

Table 4: ANOVA for response surface of MRR

Source	Sum of squares	Degrees of freedom	Mean square	*F* value	*P*-value	Remarks
Model	24.49498	27	0.907222	5462.061	<0.0001	Significant
A-on time	4.836921	1	4.836921	29121.4	<0.0001	
B-off time	7.86149	1	7.86149	47331.26	<0.0001	
C-voltage	0.021313	1	0.021313	128.3205	<0.0001	
D-current	5.732185	1	5.732185	34511.46	<0.0001	
E-tool	0.152528	1	0.152528	918.3161	<0.0001	
F-w/p	0.020881	1	0.020881	125.7164	<0.0001	
AB	0.049063	1	0.049063	295.3897	<0.0001	
AC	0.000176	1	0.000176	1.058317	0.3139	
AD	0.073632	1	0.073632	443.3125	<0.0001	
AE	0.00816	1	0.00816	49.12867	<0.0001	
Residual	0.003986	24	0.000166			
Lack of fit	0.003551	17	0.000209	3.362677	0.0545	Not significant
Pure error	0.000435	7	6.21×10^{-05}			
Cor total	24.49897	51				
Std Dev.	0.012887789		*R*-squared	0.999837288		
Mean	1.422403846		Adj *R*-squared	0.999654236		
CV%	0.906056963		Pred *R*-squared	0.99875968		
PRESS	0.030386566		Adeq precision	291.2370801		

Table 5: ANOVA for response surface of SR

Source	Sum of squares	Degree of freedom	Mean square	*F* value	*P*-value	Remarks
Model	33.66	24	1.4	301.18	<0.0001	Significant
Pulse on time	5.81	1	5.81	1247.53	<0.0001	
Pulse off time	0.12	1	0.12	26.11	<0.0001	
Voltage	0.59	1	0.59	127.1	<0.0001	
Current	0.23	1	0.23	49.07	<0.0001	
Workpiece	0.67	1	0.67	144.62	<0.0001	
AB	0.35	1	0.35	75.57	<0.0001	
AC	0.098	1	0.098	21.01	<0.0001	
AD	0.24	1	0.24	50.83	<0.0001	
Residual	0.13	27	4.66×10^{-03}			
Lack of fit	0.11	20	5.59×10^{-03}	2.8	0.0833	Not significant
Pure error	0.014	7	1.99×10^{-03}			
Std Dev.	0.068		*R*-squared	0.9963		
Mean value	3.95		Adequate *R*-squared	0.993		
C.V%	1.73		Predicted *R*-squared	0.9846		
PRESS	0.52		Adequate precision	62.564		

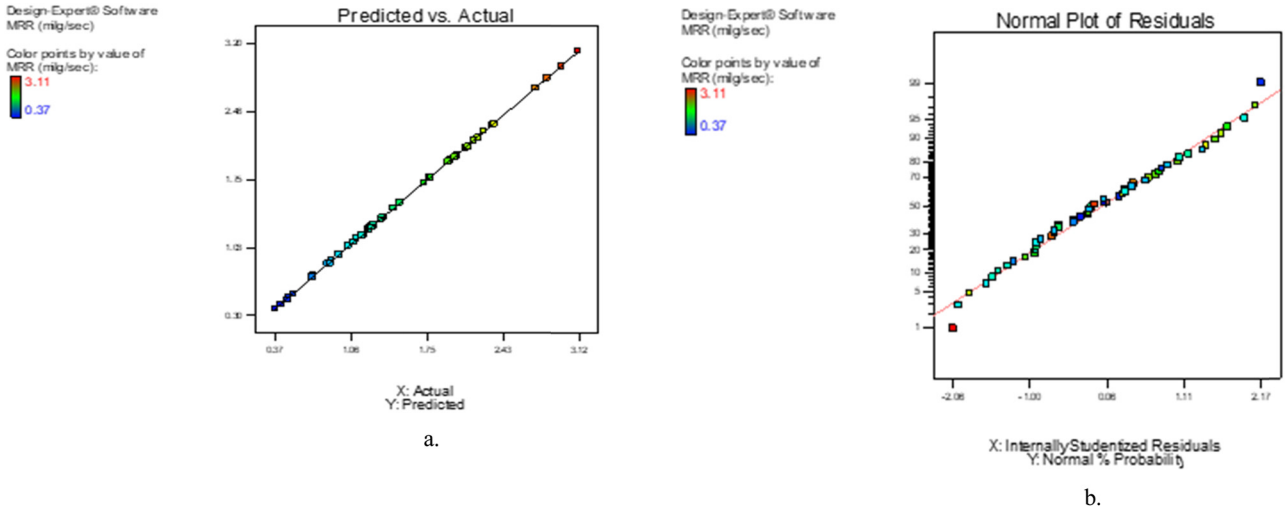

Figure 9: (a) Predicted vs actual plot of MRR and (b) normal probability plot for MRR.

because of noise. The value of "Prob. > *F*" for lack of fit 0.0545 ≫ 0.05, specifies with the aim that lack of fit is still insignificant. Non-significant lack of fit was excellent.

The *R*-squared value, which was assessed of a fraction of overall variability elucidated through the model, is equivalent to 0.999837288 ≅ 1, and is invariably wanted. The adjusted *R*-squared value is equivalent to 0.999654236; it is most valuable while contrasting models amid a diverse number of terms. The outcome illustrates that adj. *R*-squared value (0.999654236) ≅ *R*-squared value (0.999837288). Adequate precision value is equal to 291.2370801, which is signal to noise (S/N) ratio; a proportion larger than four was advantageous, which signifies plenty of model discrimination.

A quadratic regression mathematical model has been developed employing the RSM approach for predicting MRR based on the coded assets and actual assets following the elimination of non-significant terms as illustrated by equations (3) and (4).

$$\begin{aligned}\mathrm{MRR}(\mathrm{g\cdot min^{-1}}) = {} & +7.93422 + 0.02014 \times \text{on time} \\ & - 0.0476 \times \text{off time} - 0.5528 \\ & \times \text{voltage} - 0.889 \times \text{current} \\ & - 0.0330 \times \text{tool} - 0.15730 \times w/p \\ & - 4.41 \times 10^{-5} \times \text{on time} \times \text{off time} \\ & - 8.20833 \times 10^{-4} \times \text{on time} \\ & \times \text{current(in coded terms)},\end{aligned} \tag{3}$$

$$\begin{aligned}\text{MRR}(\text{g}\cdot\text{min}^{-1}) = {} & +0.86 + 0.36 \times A - 0.46 \times B - 0.023 \times C \\ & + 0.39 \times D + 0.065 \times E + 0.023 \times F \\ & - 0.040 \times A \times B - 0.049 \times A \times D \\ & + 0.016 \times A \times E - 4.312E - 003 \times A \times F \\ & + 0.055 \times B \times C - 0.049 \times B \times D \\ & - 0.034 \times B \times E + 0.025 \times B \times F \\ & + 0.011 \times C \times D + 3.875E - 003 \times C \times E \\ & + 0.018 \times D \times E + 0.023 \times D \\ & \times F (\text{In actual factors}).\end{aligned} \tag{4}$$

A diagram of the actual against the predicted response values for MRR is depicted in Figure 9(a). It helps you detect a value, or group of values, that are not easily predicted by the model. Based on the graph, we can observe that the entirety of the statistical records is based on a 45° line divided uniformly by the entire dataset.

To analyze the feasibility and practicality of the hypothesis of analysis of variance for residuals, the usual normal probability plot of the residuals for MRR is shown in Figure 9(b). The normal probability plot demonstrates whether the residuals pursue normal distribution [83,84]. If the residuals trail a normal distribution, the most extreme number of focuses should drop on a straight line. If the residuals were falling external to the straight line, it means that the residuals not entirely following the typical conveyance normal distribution [85,86].

5.1.1 Parametric interaction effect on MRR

The interaction between process parameters has a significant effect on MRR. From the 3D process graphs in Figure 10(a)–(c),

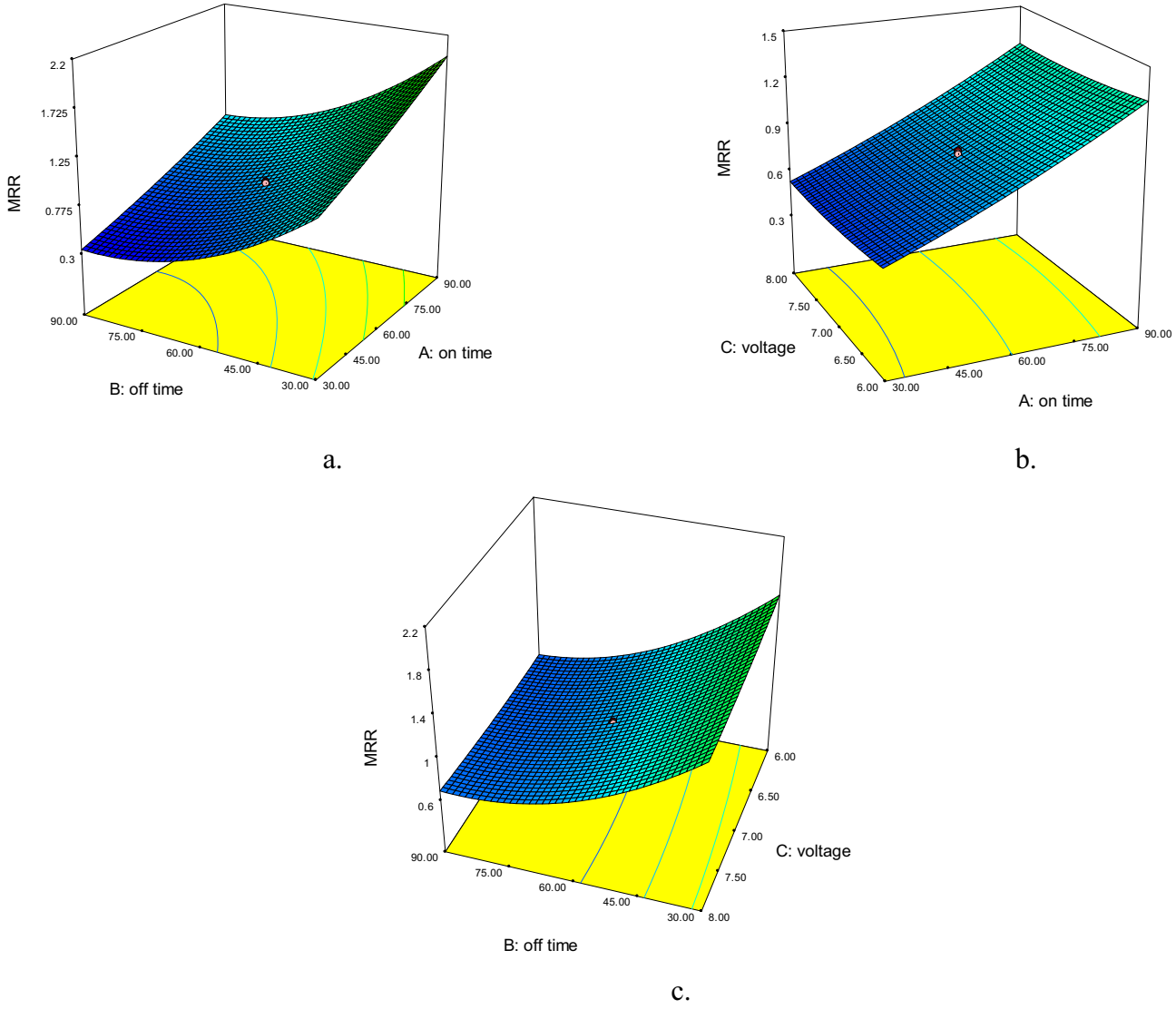

Figure 10: (a) Interaction effect of P_{on} and P_{off} on MRR, (b) interaction influence of voltage and P_{on} on MRR and (c) interaction effect of voltage and P_{off} on MRR.

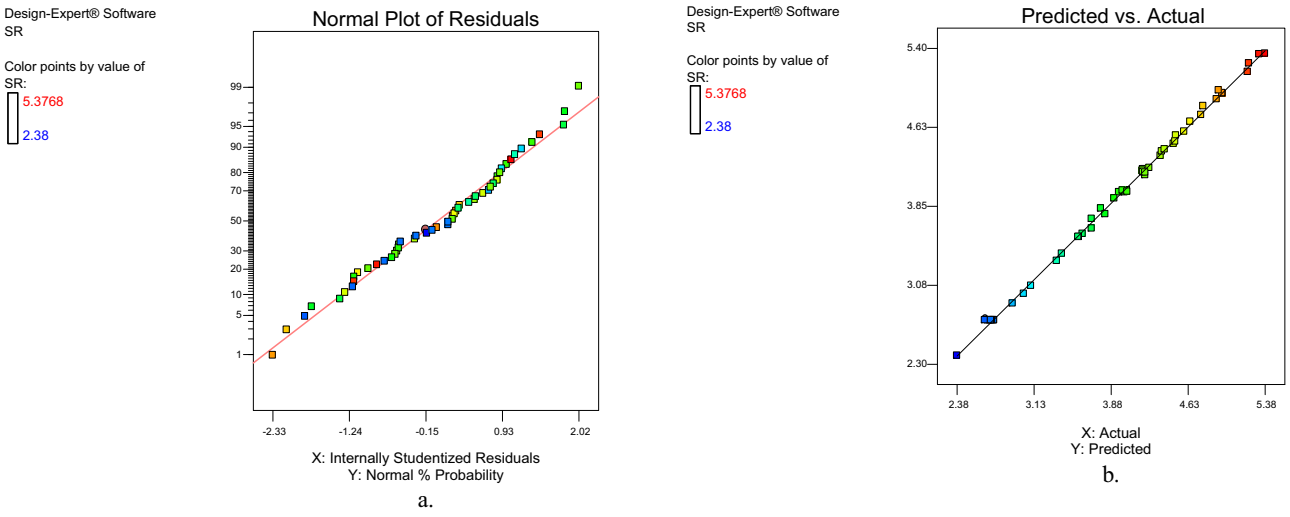

Figure 11: (a) Normal vs residual probability plot of SR and (b) predicted vs actual response values graph for SR.

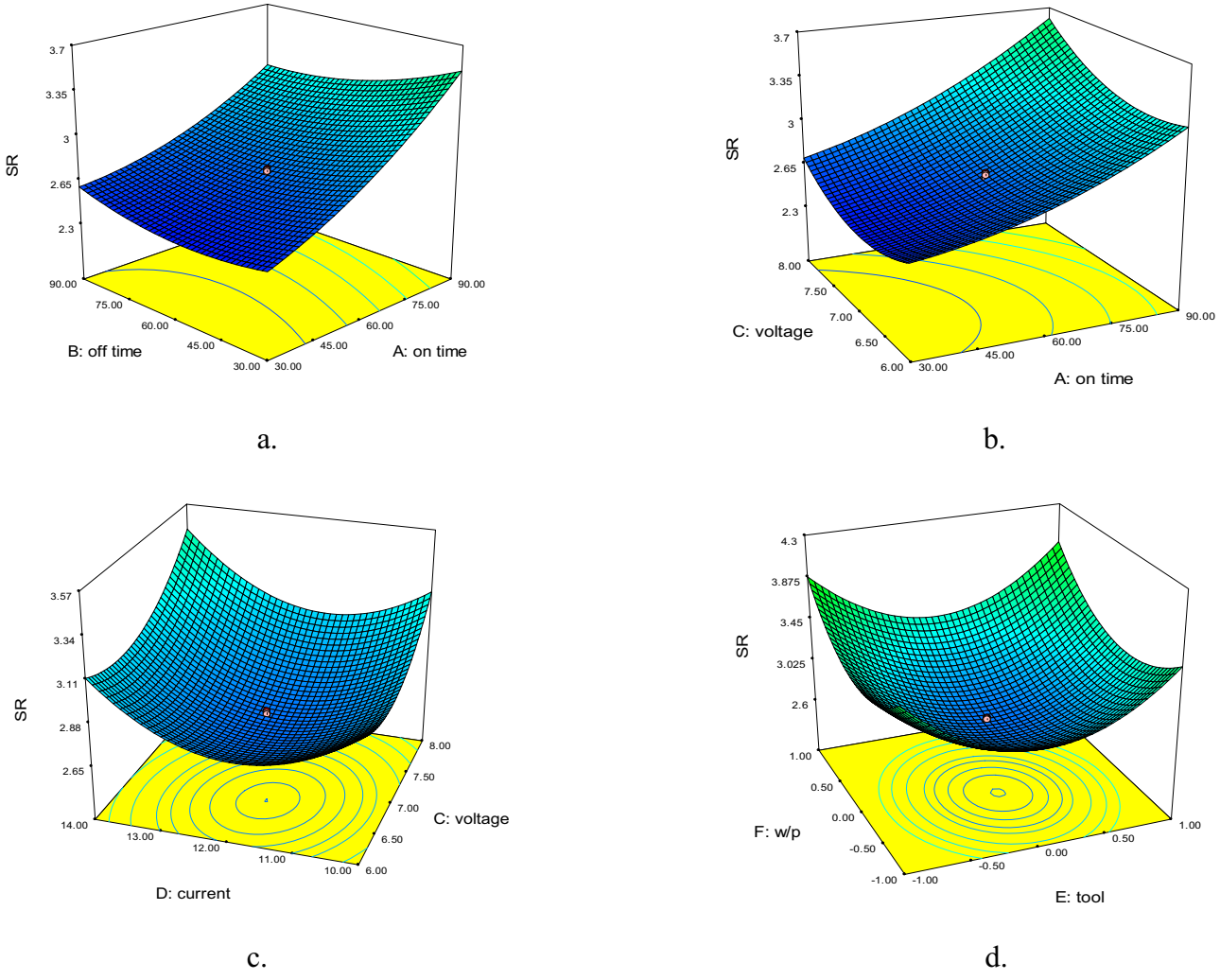

Figure 12: (a) Interaction effect of P_{on} and P_{off} on SR height (R_a in µm), (b) interaction influence of voltage and P_{on} on SR height (R_a in µm), (c) interaction influence of voltage and current on SR height (R_a in µm), and (d) interaction effect of workpiece and tool material on SR height (R_a in µm).

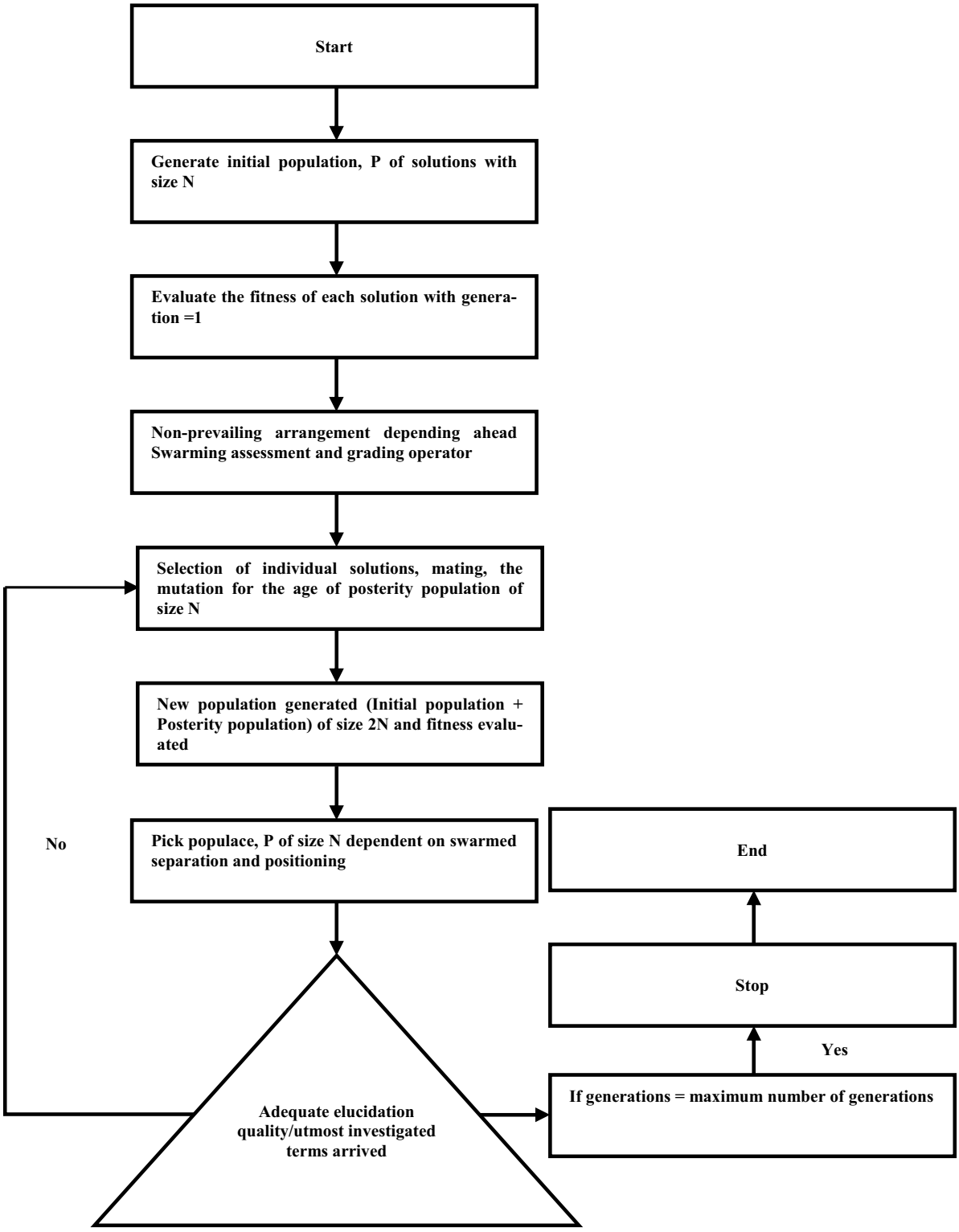

Figure 13: NSGA-II genetic algorithm.

it was clarified that with the increase in pulse on time and current, the intensity of MRR also increases, while on the other side, by enhancement of P_{off}, the MRR reduces and there is no notable effect of voltage.

5.2 Analysis of SR

All experiments conducted involves machining as per design matrix followed by MRR and SR while EDM. The

machining operation EDM has been carried out on hybrid composite workpieces using steel 304, pure copper, and brass rods of diameter 12 mm as an electrode during EDM. The average centerline SR value (R_a) of finish-machined parts has been measured using the ISR-S400 instrument.

Table 5 shows the analysis of variance for the SR quadratic model. The R-squared value, which was assessed of a fraction of total variability explicated via model, equivalent to $0.9963 \cong 1$ is invariably desirable. The adjusted R-squared value is equal to 0.993; it is most valuable while contrasting models amid a different quantity of terms. The outcome exemplifies that the adj. R-squared value (0.993) $\cong$ R-squared value (0.9963). Ample exactitude asset was equivalent to 62.564, which is a S/N ratio; a fraction superior to 4 was enviable, which shows an ample model prejudice.

After eliminating the non-significant terms from equations (5) and (6), our quadratic regression model was derived based on RSM for correlating the SR in codes of provisioned assets and actual assets with machining parameters.

$$\begin{aligned} \mathrm{SR}(\mu\mathrm{m}) = {} & +23.42764 - 0.025473 \times \text{on time} \\ & - 8.07657 \times 10^{-3} \times \text{off time} \\ & - 2.66761 \times \text{voltage} - 1.89322 \times \text{current} \\ & - 0.059175 \times \text{tool(in coded terms)}, \end{aligned} \tag{5}$$

$$\begin{aligned} \mathrm{SR}(\mu\mathrm{m}) = {} & + 2.73 + 0.40 \times 0.056 \times B + 0.13 \times C \\ & + 0.075 \times D - 0.014 \times E + 0.14 \times F \\ & - 0.11 \times A \times B + 0.057 \times A \times C \\ & + 0.087 \times A \times D - 0.049 \times A \\ & \times F - 0.039 \times B \times C + 0.043 \times B \times D \\ & + 0.050 \times B \times F + 0.026 \times C \times D \\ & + 0.039 \times C \times E - 0.038 \times D \times E \\ & - 0.033 \times D \times F + 0.023 \times E \\ & \times F(\text{in actual factors}). \end{aligned} \tag{6}$$

To scrutinize the feasibility of the hypothesis of analysis of variance for residuals, the typical likelihood standard probability plot of the residuals for SR is shown in Figure 11(a). Normal vs residual probability plot of SR demonstrates whether the residuals trail a typical dispersion based normal probability [38,87,88].

If residuals follow a standard normal probability distribution, the utmost volume of spots should drop on a straight line contour, and the comparable findings have been unveiled [39,89,90]. If residuals were descending exterior to the outer surface straight line, it implies not entirely following a normal distribution. Figure 11(b) exhibits the predicted vs actual graph for SR.

The findings have concluded that the residuals drop on a straight line inferring that the residuals were dispersed ordinarily.

5.2.1 Parametric interaction effect on SR

EDM is known for its accuracy and high surface quality [41,91,92]. A good response output is an interaction effect of input parameters. Figure 12 depicts some graphs for significant interaction effect on SR-based response characteristics. From Figure 12(a)–(d), it replicates that surface quality deteriorates at superior assets of P_{on}, whereas by the means of an increase in P_{off} there is a significant improvement in surface quality. Voltage is also a significant factor as SR height amplifies with enhancement in voltage, whereas, SR is low during machining second workpiece material. SR value is minimum at a low value of voltage and current, i.e., at 6.5 V and 12 A. Thereafter, the roughness height increases with the increase in current and voltage. Interaction effect of workpiece material and tool material have a significant effect on SR. Copper as tool material and second workpiece material has a lower SR heights.

The comparable outcomes have been unveiled by Khajuria et al., where they have reported that the MRR, TWR, and SR all had enhanced when the current and P_{on} have been raised [93]. Findings have exhibited lesser TWR but a superior surface quality has been accomplished when the current, P_{on}, and voltage were all adjusted to their optimal values for AA-2014/Al_2O_3 composites. Creep-behavior of the welded heat-affected zone (HAZ) of boron-free P-91 (PM) and boron-modified P-91-B (B-PM) steels were explored by Khajuria et al. [94]. Outcomes have been discovered that by incorporating 100 ppm of boron to standard P-91 steel enhanced creep-rupture-ductileness, which in turn deferred type-IV breakdowns in HAZs of P-91 steel-welded joints. Throughout EDM machining of stir-casted AA-2014 composite materials, Khajuria et al. have investigated the influence of variability

Table 6: Drivers or actuators utilized during NSGA-II

Sr. no.	Operator	Type	Value
1	Population size	—	100
2	Number of generations	—	1,000
3	Crossover	Simulated binary	0.8
4	Mutation	Polynomial	0.2
5	Selection	Non-dominating sorting and crowding distance	—

Table 7: Solution set suggested by NSGA-II

Sr no.	T_{on}	T_{off}	Voltage	Current	Tool	Workpiece	SR	MRR
1	30.0559	88.17259	7.998975	13.58342	−0.12544	−0.98413	−21.1831	0.470727
2	30.00903	83.44194	7.291668	10.24155	−0.0124	−0.09539	−13.9603	0.128558
3	30.68383	89.2314	7.999376	12.85318	−0.18521	−0.91374	−24.4379	1.141943
4	30.02465	83.53458	7.984257	12.16802	−0.03812	−0.51002	−19.9216	0.321807
5	30.00903	84.48689	6.772159	10.00125	0.005715	−0.10183	−16.5914	0.154659
6	30.02661	89.22198	7.998884	13.84435	−0.18521	−0.91374	−21.5216	0.518039
7	30.0813	89.22242	7.999988	13.58002	−0.13382	−0.75166	−14.8322	0.131788
8	30.02513	84.49668	7.998548	12.75501	−0.02482	−0.31629	−23.318	0.829139
9	30.02596	89.22611	7.999086	13.99565	−0.77095	−0.95462	−22.7397	0.720066
10	30.02465	83.3961	7.995625	10.01966	−0.08786	−0.16131	−23.8303	0.954423
11	30.16198	84.4886	7.999995	12.4	−0.16188	−0.70887	−22.162	0.616704
12	30.0093	89.21858	7.999647	13.99742	−0.39597	−0.98991	−15.4845	0.138252
13	30.05702	84.4894	6.775895	10.06707	−0.01345	−0.1644	−20.9311	0.448893
14	30.02465	88.86023	7.999427	13.96865	−0.65709	−0.97172	−20.2732	0.357794
15	30.00903	83.43818	7.999235	12.4	−0.04594	−0.97172	−23.6028	0.895679
16	30.02661	84.49681	7.098247	10.01966	−0.08786	−0.16131	−21.5337	0.544917
17	30.0091	89.21827	7.999882	13.98641	−0.86097	−0.99577	−19.6998	0.309399
18	30.0093	84.49717	7.998177	11.61248	−0.15289	−0.90287	−16.464	0.152951
19	30.15356	83.39415	7.99998	12.16822	0.010258	−0.70835	−20.4923	0.40178
20	30.0093	84.49717	7.998177	10.62443	−0.02409	−0.31818	−24.4119	1.108837
21	30.02512	83.53458	7.983769	12.16837	−0.03762	−0.91427	−24.4783	1.187697
22	30.01708	81.69032	7.893018	10.0015	−0.02502	−0.09444	−20.4159	0.375745
23	30.00903	83.44271	7.999859	11.61277	−0.15191	−0.7084	−21.3794	0.506632
24	30.02694	84.48774	7.999914	13.40785	−0.15242	−0.91374	−23.1921	0.800603
25	30.15356	83.39415	7.998548	10.24287	−0.08691	−0.16131	−17.5873	0.175732
26	30.00942	83.3961	7.99885	10.24204	-7.97×10^{-05}	−0.15778	−23.3346	0.856275
27	30.02596	83.50303	7.99885	10.24204	−0.03788	−0.5098	−18.9049	0.240512
28	30.02465	83.3961	7.999235	12.4	−0.03812	−0.51002	−14.9595	0.133293
29	30.1614	83.37566	7.999952	11.33627	-7.97×10^{-05}	−0.15778	−16.9364	0.161107
30	30.68612	89.2314	7.999235	12.40059	−0.16285	−0.53129	−24.3167	1.047891
31	30.01684	88.17259	7.998975	13.58342	−0.12495	−0.97156	−22.6062	0.709093
32	30.02661	89.22198	7.999274	13.84386	−0.1849	−0.99674	−19.4409	0.278317
33	30.02944	89.21854	7.999778	10.90246	−0.0124	−0.31874	−24.424	1.139366
34	30.01684	84.49668	7.998901	12.95635	−0.39586	−0.98967	−18.6056	0.226207
35	30.01684	84.49668	7.998548	12.95732	−0.39597	−0.98991	−15.5347	0.141403
36	30.00903	88.17259	7.998975	13.99961	−0.15669	−0.71	−14.1277	0.129611
37	30.0093	84.49717	7.999857	11.92279	−0.23707	−0.16521	−13.9603	0.128558
38	30.08141	88.17024	7.999613	13.75535	−0.23796	−0.53129	−24.3711	1.077797
39	30.00903	83.3961	7.999006	12.75501	−0.15602	−0.70838	−21.8624	0.565486
40	30.08093	88.17024	7.999613	13.75535	−0.23796	−0.98967	−24.0653	0.980265
41	30.15386	83.39439	7.995625	11.61248	−0.15289	−0.16521	−22.389	0.659426
42	30.0093	82.02168	7.267655	10.01975	−0.02514	−0.08791	−19.6896	0.308993
43	30.02465	89.21858	7.999647	13.75582	−0.15653	−0.71049	−17.7661	0.185878
44	30.0093	83.3961	7.995625	10.90248	−0.0124	−0.1438	−16.1035	0.147647
45	30.16193	88.16931	7.999613	13.40882	−0.16139	−0.70702	−20.0394	0.34828
46	30.03185	81.68251	7.893995	10.90248	−0.0124	−0.1438	−24.4534	1.176383
47	30.0093	84.49668	7.998548	13.22133	−0.02445	−0.91427	−15.9574	0.14369
48	30.01684	89.21858	7.999647	13.99961	−0.15242	−0.90205	−18.9647	0.242042
49	30.02596	89.22611	7.999086	13.99565	−0.16188	−0.97156	−22.8502	0.735165
50	30.68481	88.07271	7.998548	11.33627	−0.03776	−0.5315	−21.9886	0.597481
51	30.02596	83.50303	7.999778	10.90246	−0.0124	−0.31874	−23.5297	0.893173
52	30.02944	89.21854	7.999613	11.61248	−0.0236	−0.31825	−23.7682	0.930905
53	30.0559	88.17259	7.998548	12.95684	−0.18603	−0.91427	−24.1009	0.996277
54	30.0559	88.17259	7.998975	13.58342	−0.04594	−0.31629	−14.4539	0.130842
55	30.02465	83.39415	7.99998	12.16822	0.010258	−0.70835	−17.3073	0.168812
56	30.026	81.6914	7.97913	10.59397	0.00075	−0.08791	−21.6886	0.545571

(*Continued*)

Table 7: *Continued*

Sr no.	T_{on}	T_{off}	Voltage	Current	Tool	Workpiece	SR	MRR
57	30.68383	89.2314	7.999376	12.85318	−0.18521	−0.98413	−22.8972	0.760598
58	30.68383	89.2314	7.999376	12.85318	−0.18521	−0.71049	−23.6294	0.925698
59	30.0093	81.6914	7.979374	11.16822	−0.08642	−0.16131	−18.0186	0.193158
60	30.0093	84.49717	7.998177	11.61248	−0.15289	−0.70838	−22.5028	0.676961
61	30.02661	89.21858	7.999648	13.99961	−0.86097	−0.99674	−19.1565	0.271524
62	30.15288	83.39516	7.575015	10.24498	−0.08728	−0.16111	−19.4961	0.285213
63	30.01709	82.02208	7.267848	10.02073	−0.02418	−0.0871	−24.135	1.041988
64	30.02671	89.22618	7.999086	13.99581	−0.77192	−0.95462	−24.3335	1.069649
65	30.01024	88.17357	7.998975	13.58342	−0.03812	−0.51002	−21.9613	0.59187
66	30.00832	84.49717	7.998177	13.22031	−0.02641	−0.7085	−20.7321	0.415504
67	30.68612	89.2314	7.999236	12.40059	−0.16285	−0.97221	−18.4125	0.209227
68	30.00942	83.43857	7.046576	10.00169	−0.02281	−0.10244	−22.2404	0.6391
69	30.08093	88.17024	7.999613	13.75535	−0.23699	−0.9012	−19.0775	0.26211
70	30.02567	84.49682	7.999158	12.75509	−0.0258	−0.31629	−23.4251	0.86142

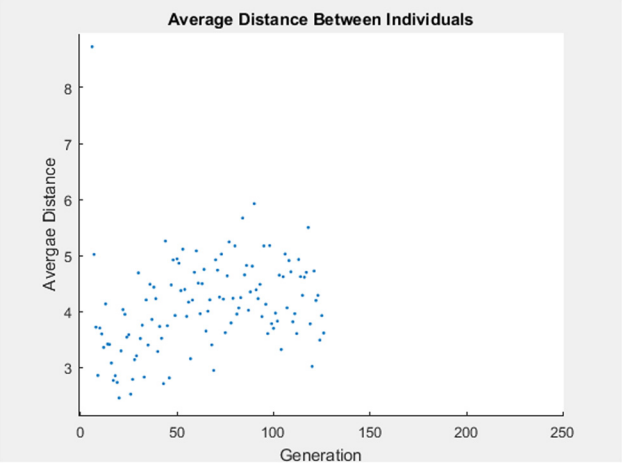

Figure 14: The initial solution set of 200 generations.

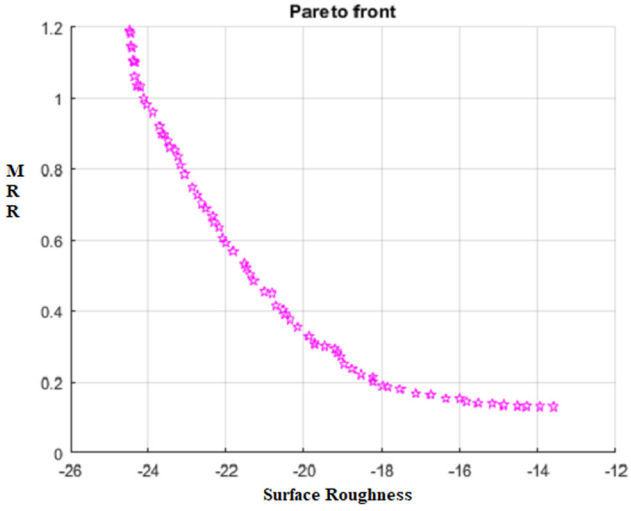

Figure 15: Pareto optimal solution of NSGA-II.

within wt% of ceramic-alumina as reinforcing particulates [95]. The MRR and SR were found to be lower when the wt% of ceramic-alumina particulates were raised; however, the TWR was observed to be escalated [42,43,95].

Table 8: Confirmation experiments and results

S. no.	T_{on} (µs)	T_{off} (µs)	I_P (A)	V_g (V)	Tool	Workpiece	Actual values		Predicted values		Error (%)	
							MRR (g·min^{-1})	SR (µm)	MRR (g·min^{-1})	SR (µm)	MRR (g·min^{-1})	SR (µm)
1.	30.0	88	7.99	13.5	−0.1	−0.9	0.3714	0.45	0.3531	0.47	−4.92	−4.2
2.	30.0	83	7.29	10.2	−0.0	−0.0	0.2318	0.122	0.2327	0.128	+4.12	−4.6
3.	30	88	7.9	13.7	−0.2	−0.9	0.3105	0.27	0.3180	0.26	+2.30	+3.7
4.	30	84	7.9	12.7	−0.0	−0.3	0.3784	0.82	0.3904	0.86	−3.07	−4.6

6 Multi-response optimization using Non-dominating Sorted Genetic Algorithm-II (NSGA-II)

The major goal of the present research was to optimize EDM factors for the desired output responses. Both the responses in this study are conflicting as an increase in MRR will result in poor surface quality but in manufacturing work, an increase in MRR is desirable to meet production output. Hence, to set up a compromise is must between output responses to preserve superiority and extent. Further, NSGA-II is used to establish a most favorable stipulation for mutual responses as shown in Figure 13. Table 6 shows several operators used during NSGA-II analysis and Table 7 illustrates a set of solutions suggested by NSGA-II.

$$\text{Objective 1} = \text{SR}, \tag{7}$$

$$\text{Objective 2} = 1/\text{MRR or } (-\text{MRR}). \tag{8}$$

With the assistance of NSGA-II, the factual Pareto ideal elucidations can be acquired by keeping up exclusivity in the outcomes (based on the swarming separation and non-mastery grade) [96–98]. The non-subjugated results acquired toward the finishing stage of 1000 age groups or generations are shown in Figure 15. This demonstrates the creation & development of Pareto ideal facade prompting to the ultimate arrangement of results.

Thirty elucidations beyond 100 arrangements are chosen where there is a considerable variation in values of cutting rate and SR.

Table 8 demonstrates an inaccuracy amid affirmative outcomes and anticipated assets are fewer than 5%. It affirms the magnificent resemblance of the outcomes. Thus, it can safely be concluded that 70 solutions as presented in Table 7 can be used by manufacturing planners as guidelines for concurrent optimization of MRR and SR. Figure 14 shows the initial solution set. The figure discloses that the inaugural sorts of elucidations are haphazardly distributed beside the realms of cutting rate and SR and the findings have been similar with the existing studies [99–101]. On running the program, it has been perceived that nearly all analogous arrangements of explication were accomplished when the computation was kept running for 950, 960, 970, 980, 990, and 1,000 age groups or epochs. It demonstrates that the NSGA-II is suitably congregated or matched when it is kept running for 1,000 eons. The non-subjugated resolution arrangement acquired toward the finish of 1,000 epochs as appeared in Figure 15.

$$30 \le P_{\text{on}} \le 90, \tag{9}$$

$$30 \le P_{\text{off}} \le 90, \tag{10}$$

$$6 \le \text{Voltage} \le 8, \tag{11}$$

$$10 \le \text{Current} \le 14. \tag{12}$$

A total of 70 solutions as shown in Table 7 are forecasted by NSGA-II; however, none of these clarifications can be superior to another. These outcomes are comparable to those found in prior investigations [102–104]. The decision of one elucidation over alternate relies upon the prerequisite of the procedure route design. As long as the recital execution extents are clashing or contradictory in the environment, surface eminence reduces as MRR enhances and similar conduct of execution measures is viewed in the outcomes accomplished, and the related works have been published by numerous studies [105,106].

7 Conclusion

An EDM experimentation have been designed using the central composite design to investigate the effect of EDM parameters on selected responses. Validation experiments confirm the proximity of the results produced by RSM. Additionally, the model obtained can be applied to artificial intelligence. In order to ensure the fit of the models, quadratic models have been developed and followed by a validity test. Multi-objective optimization using NSGA-II has been conducted to identify the most favorable set of factors to obtain the same optimal result. A surface analysis has been completed for the tool and the workpiece to determine how operating route factors affect surface texture. As a result of these tentative trials, the following outcomes have been achieved:

i. SEM images of the tool material and workpiece material show the recast layer formed on the tool face and workpiece-machined surface.
ii. EDS analysis also exhibits the machined surface and deposition of tool material on the workpiece surface in the form of a recast layer.
iii. P_{on}, P_{off} and current have a significant effect on MRR. Gap voltage has an almost insignificant contribution. The optimal value of MRR (2.97 g·min^{-1}) has been achieved at 90 µs, 30 µs, 7.0 V, and 14 A as P_{on}, P_{off}, gap voltage, and peak current, respectively.
iv. It has been recorded that SR is commensurate to P_{on} and reciprocal proportional to P_{off}. The optimal value of SR (2.41 µm) has been achieved at 30 µs, 52 µs, 6.0 V, and 12 A as P_{on}, P_{off}, gap voltage, and peak current, respectively.

v. MRR and SR increase on increasing the value of T_{on} and current (individual and combined effect), which are two major machining parameters of EDM. Peak current, P_{on}, and P_{off} were significant and noteworthy factors influencing response output; however, gap voltages and materials of the workpiece had limited impact.
vi. On the other hand, with an increase in P_{off}, there is a decrease in MRR and also improvement in surface quality. SR increases with the increment in P_{off}. Voltage has no significant impact on both MRR and SR.
vii. An increase in the value of current results in the increase in MRR but has no significant effect on SR as initially SR decreases at 6.5 V but afterward with increment in current, SR increases.
viii. P_{off} has been revealed to be contributory parameter followed by current and P_{on} for MRR.
ix. The validity experiments confirmed that models developed for selected responses predicted results exceedingly concordant with investigational results. Based on the developed models, the output response can be expected in favor of a known set of input factors and oppositely for the desired value of output response; parametric values of input variables can be calculated in advance. In various combinations of process parameters, a developed model can effectively predict MRRs and SR heights.
x. For SR height, voltage is also a significant factor as SR height enhances with enhancement in voltage, whereas, SR is low during machining second workpiece material.
xi. In multi-objective optimization, for an optimal set of response variables, P_{on} as 30 µs, P_{off} as 30 µs, gap voltage as 6 V, and peak current as 14 A can be set as process parameters for MRR and SR.

Funding information: The authors state no funding involved.

Author contributions: Literature review and analysis have been conducted by Harish K Garg, Shubham Sharma, Rajesh Kumar, Alakesh Manna, Changhe Li, and Kuwar Mausam, along with the article's development and writing. Several aspects of the final version of the article were developed, supervised, and approved by Harish K Garg, Shubham Sharma, and Elsayed Mohamed Tag Eldin. Apart from writing the article, Shubham Sharma and Elsayed Mohamed Tag Eldin also helped with the literature review and analysis. This manuscript has been approved for submission by all authors and they accept responsibility for its content.

Conflict of interest: The authors state no conflict of interest.

Ethical approval: Human or animal participants have not been used in any of the experiments reported in this article.

Informed consent statement: Not applicable.

Data availability statement: Not Applicable.

References

[1] Allien, V. J., H. Kumar, and V. Desai. Dynamic analysis and optimization of SiC reinforced Al6082 and Al7075 MMCs. *Materials Research Express*, Vol. 6, 2019, id. 056528.
[2] Yadav, R. S. and V. Yadava. Hybrid design-based modeling and multi-objective optimization of hybrid machining of hybrid metal matrix composites. *Proceedings of the Institution of Mechanical Engineers, Part C: Journal of Mechanical Engineering Science*, Vol. 233, No. 7, 2018, pp. 2275–2301.
[3] Khullar, V. R., N. Sharma, S. Kishore, and R. Sharma. RSM- and NSGA-II-based multiple performance characteristics optimization of EDM parameters for AISI 5160. *Arabian Journal for Science and Engineering*, Vol. 42, 2017, pp. 1917–1928.
[4] Garg, H. K., K. Verma, A. Manna, and R. Kumar. Hybrid metal matrix composites and a further improvement in their machinability-A review. *International Journal of Latest Research in Science and Technology*, Vol. 1, 2012, pp. 36–44.
[5] Gopalakannan, S., T. Senthilvelan, and S. Ranganathan. Statistical optimization of EDM parameters on machining of aluminum hybrid metal matrix composite by applying Taguchi based Grey analysis. *Journal of Scientific and Industrial Research* (*India*), Vol. 72, 2013, pp. 358–365.
[6] Bodunrin, M. O., K. K. Alaneme, and L. H. Chown. Aluminium matrix hybrid composites: a review of reinforcement philosophies; mechanical, corrosion and tribological characteristics. *Journal of Materials Research and Technology*, Vol. 4, 2015, pp. 434–445.
[7] Kansal, H. K., S. Singh, and P. Kumar. Numerical simulation of powder mixed electric discharge machining (PMEDM) using finite element method. *Mathematical and Computer Modelling*, Vol. 47, 2008, pp. 1217–1237.
[8] James, S. J., K. Venkatesan, P. Kuppan, and R. Ramanujam. Hybrid aluminum metal matrix composite reinforced with SiC and TiB2. *Procedia Engineering*, Vol. 97, 2014, pp. 1018–1026.

[9] Choudhary, S. K. and R. S. Jadoun. Current advanced research development of electric discharge machining (EDM): A review. *International Journal of Research in Advent Technology*, Vol. 2, 2014, pp. 273–297.
[10] Sarkar, A., S. C. Panja, D. Das, and B. Sarkar. Developing an efficient decision support system for non-traditional machine selection: an application of MOORA and MOOSRA. *Production and Manufacturing Research*, Vol. 3, 2015, pp. 324–342.
[11] Kumar, S. S., M. Uthayakumar, S. T. Kumaran, and P. Parameswaran. Electrical discharge machining of Al(6351)-SiC-B_4C hybrid composite. *Materials and Manufacturing Processes*, Vol. 29, 2014, pp. 1395–1400.
[12] Beri, N., S. Maheshwari, C. Sharma, and A. Kumar. Technological advancement in electrical discharge machining with powder metallurgy processed electrodes: A review. *Materials and Manufacturing Processes*, Vol. 25, 2010, pp. 1186–1197.
[13] Ghosal, A., A. Manna, and A. K. Lall. Modelling of Ytterbium Fiber Laser parameters during micromachining of Al-15wt% Al_2O_3-MMC. *Procedia Engineering*, Vol. 90, 2014, pp. 704–709.
[14] Garg, S. K., A. Manna, and A. Jain. Experimental investigation of spark gap and material removal rate of Al/ZrO_2(P)-MMC machined with wire EDM. *Journal of the Brazilian Society of Mechanical Sciences and Engineering*, Vol. 38, 2016, pp. 481–491.
[15] Singh, J. and A. Chauhan. Characterization of hybrid aluminum matrix composites for advanced applications – A review. *Journal of Materials Research and Technology*, Vol. 5, 2016, pp. 159–169.
[16] Bhandare, R. G. and P. M. Sonawane. Preparation of aluminium matrix composite by using stir casting method. *International Journal of Engineering and Advanced Technology*, Vol. 3, 2013, pp. 61–65.
[17] Ciftci, I., M. Turker, and U. Seker. CBN cutting tool wear during machining of particulate reinforced MMCs. *Wear*, Vol. 257, 2004, pp. 1041–1046.
[18] Sharma, V., U. Prakash, and B. V. M. Kumar. Surface composites by friction stir processing: A review. *Journal of Materials Processing Technology*, Vol. 224, 2015, pp. 117–134.
[19] Srivastava, A., P. Garg, A. Kumar, and Y. Krishna. A review on fabrication & characterization of hybrid aluminium metal matrix composite. *International Journal of Advance Research and Innovation*, Vol. 1, 2014, pp. 242–246.
[20] Kulkarni, A. S., K. C. Hegade, O. V. Karale, and P. S. Joshi. Coupled thermal and structural analysis of brake disc rotor manufactured from aluminum metal matrix composite (AMMC) reinforced with silicon carbide. *Imperial Journal of Interdisciplinary Research*, Vol. 2, 2016, pp. 1188–1194.
[21] Chohan, J. S., N. Mittal, R. Kumar, S. Singh, S. Sharma, S. P. Dwivedi, et al. Optimization of FFF process parameters by naked mole-rat algorithms with enhanced exploration and exploitation capabilities. *Polymers*, Vol. 13, No. 11, 2021, id. 1702.
[22] Kumar, J., D. Singh, N. S. Kalsi, S. Sharma, C. I. Pruncu, D. Y. Pimenov, et al. Comparative study on the mechanical, tribological, morphological and structural properties of vortex casting processed, Al-SiC-Cr hybrid metal matrix composites for high strength wear-resistant applications: Fabrication and characterizations. *Journal of Materials Research and Technology*, Vol. 9, No. 6, 2020, pp. 13607–13615.
[23] Dwivedi, S. P., A. Saxena, and S. Sharma. Influence of nano-CuO on synthesis and mechanical behavior of spent alumina catalyst and grinding sludge reinforced aluminum based composite. *International Journal of Metalcasting*, Vol. 16, 2021, pp. 292–303.
[24] Sivalingam, P., V. Krishnaraj, S. Sharma, S. K. Mouleeswaran, R. J. Kumar, and R. Zitoune. Experimental study on thermal and morphological analysis of green composite sandwich made of flax and agglomerated cork. *Journal of Thermal Analysis and Calorimetry*, Vol. 139, 2020, pp. 3003–3012.
[25] Muni, R. N., J. Singh, V. Kumar, and S. Sharma. Parametric optimization of rice husk ash, copper, magnesium reinforced aluminium matrix hybrid composite processed by EDM. *ARPN Journal of Engineering and Applied Science*, Vol. 14, No. 22, 2019, pp. 1828–1834.
[26] Muni, R. N., J. Singh, V. Kumar, and S. Sharma. Influence of rice husk ash, Cu, Mg on the mechanical behaviour of Aluminium Matrix hybrid composites. *International Journal of Applied Engineering Research*, Vol. 14, No. 8, 2019, pp. 1828–1834.
[27] Dwivedi, S. P., A. Saxena, S. Sharma, A. K. Srivastava, and N. K. Maurya. Influence of SAC and eggshell addition in the physical, mechanical and thermal behaviour of Cr reinforced aluminium based composite. *International Journal of Cast Metals Research*, Vol. 34, No. 1, 2021, pp. 43–55.
[28] Saxena, A., S. P. Dwivedi, A. Dixit, S. Sharma, A. K. Srivastava, and N. K. Maurya. Computational and experimental investigation on mechanical behavior of zirconia toughened alumina and nickel powder reinforced EN31 based composite material. *Materialwissenschaft und Werkstofftechnik*, Vol. 52, No. 5, 2021, pp. 548–560.
[29] Sharma, S., J. Singh, M. K. Gupta, M. Mia, S. P. Dwivedi, A. Saxena, et al. Investigation on mechanical, tribological and microstructural properties of Al-Mg-Si-T6/SiC/muscovite-hybrid metal-matrix composites for high strength applications. *Journal of Materials Research and Technology*, Vol. 12, No. 21, 2021, pp. 1564–1581.
[30] Dwivedi, S. P., R. Agrawal, and S. Sharma. Effect of friction stir process parameters on mechanical properties of chrome containing leather waste reinforced aluminium based composite. *International Journal of Precision Engineering and Manufacturing-Green Technology*, Vol. 8, No. 3, 2021, pp. 935–943.
[31] Kumar, J., D. Singh, N. S. Kalsi, S. Sharma, J. Mia, M. Singh, et al. Investigation on the mechanical, tribological, morphological and machinability behavior of stir-casted Al/SiC/Mo reinforced MMCs. *Journal of Materials Research and Technology*, Vol. 12, 2021, pp. 930–946.
[32] Aggarwal, V., J. Singh, S. Sharma, A. Sharma, G. Singh, J. Parshad. Empirical modeling of machining parameters during WEDM of Inconel 690 using response surface methodology. *AIP Conference Proceedings*, Vol. 2281, 2020, id. 020032.
[33] Aggarwal, V., J. Singh, S. Sharma, K. Harish, A. Garg, G. Sharma, et al. An experimental study of wire breakage

frequency on different electrodes during WEDM of Inconel-722. *IOP Conference Series: Materials Science and Engineering*, Vol. 954, 2020, id. 12013.

[34] Aggarwal, V., C. I. Pruncu, J. Singh, S. Sharma, and D. Y. Pimenov. Empirical investigations during WEDM of Ni-27Cu-3.15Al- 2Fe-1.5Mn based superalloy for high temperature corrosion resistance applications. *Materials*, Vol. 13, No. 16, 2020, id. 3470.

[35] Qureshi, M. N., S. Sharma, J. Singh, S. D. A. Khadar, and R. U. Baig. Evaluation of surface roughness in the turning of mild steel under different cutting conditions using back propagation neural network. *Proceedings of the Estonian Academy of Sciences*, Vol. 69, 2020, pp. 109–115.

[36] Islam, S., S. P. Dwivedi, V. K. Dwivedi, S. Sharma, and D. Kozak. Development of marble dust/waste PET based polymer composite material for environmental sustainability: fabrication and characterizations. *Journal of Materials Performance and Characterization*, Vol. 10, No. 1, 2021, pp. 538–552.

[37] Alaneme, K. K. and K. O. Sanusi. Microstructural characteristics, mechanical and wear behaviour of aluminium matrix hybrid composites reinforced with alumina, rice husk ash and graphite. *Engineering Science and Technology, an International Journal*, Vol. 18, No. 3, 2015, pp. 416–422.

[38] Bisaria, H. and P. Shandilya. Wire electric discharge machining induced surface integrity for Ni55.95Ti44.05 shape memory alloy. *Proceedings of the Institution of Mechanical Engineers, Part E: Journal of Process Mechanical Engineering*, Vol. 235, No. 2, 2020, pp. 178–185.

[39] Arora, G. and S. Sharma. A comparative study of AA6351 mono-composites reinforced with synthetic and agro waste reinforcement. *International Journal of Precision Engineering and Manufacturing*, Vol. 19, 2018, pp. 631–638.

[40] Shaikh, M. B., T. Aziz, S. Arif, A. H. Ansari, P. G. Karagiannidis, and M. Uddin. Effect of sintering techniques on microstructural, mechanical and tribological properties of Al-SiC composites. *Surfaces and Interfaces*, Vol. 20, 2020, id. 100598.

[41] Alhodaib, A., P. Shandilya, A. K. Rouniyar, and H. Bisaria. Experimental Investigation on Silicon Powder Mixed-EDM of Nimonic-90 Superalloy. *Metals*, Vol. 11, No. 11, 2021, id. 1673.

[42] Bisaria, H. and P. Shandilya. Surface integrity aspects for NiTi shape memory alloys during wire electric discharge machining: A review. *Journal of Materials Research*, Vol. 35, 2020, pp. 537–558.

[43] Bisaria, H. and P. Shandilya. Experimental investigation on wire electric discharge machining (WEDM) of Nimonic C-263 superalloy. *Materials and Manufacturing Processes*, Vol. 34, 2018, pp. 83–92.

[44] Sharma, S., P. Sudhakara, J. Singh, R. A. Ilyas, M. R. M. Asyraf, and M. R. Razman. Critical review of biodegradable and bioactive polymer composites for bone tissue engineering and drug delivery applications. *Polymers*, Vol. 13, No. 6, 2021, id. 2623.

[45] Ilyas, R. A., S. M. Sapuan, M. R. M. Asyraf, D. A. Z. N. Dayana, J. J. N. Amelia, M. S. A. Rani, et al. Polymer composites filled with metal derivatives: a review of flame retardants. *Polymers*, Vol. 13, 2021, id. 1701.

[46] Sharma, S., P. Sudhakara, A. Borhana, J. Singh, and R. A. Ilyas. Recent trends and developments in conducting polymer nanocomposites for multifunctional applications. *Polymers*, Vol. 13, No. 17, 2021, id. 2898.

[47] Sharma, S. and P. Sudhakara. Fabrication and optimization of hybrid AA-6082-T6 alloy/8%Al_2O_3(Alumina)/2%Grp metal matrix composites using novel Box-Behnken methodology processed by wire-sinking electric discharge machining. *Materials Research Express*, Vol. 6, 2019, id. 116594.

[48] Singh, Y., J. Singh, S. Sharma, T. D. Lam, and D. N. Nguyen. Fabrication and characterization of coir/carbon-fiber reinforced epoxy based hybrid composite for helmet shells and sports-goods applications: influence of fiber surface modifications on the mechanical, thermal and morphological properties. *Journal of Materials Research and Technology*, Vol. 20, 2020, id. 31989.

[49] Singh, Y., J. Singh, S. Sharma, V. Aggarwal, and C. I. Pruncu. Multi-objective optimization of Kerf-taper and surface-roughness quality characteristics for cutting-operation on coir and carbon fibre reinforced epoxy hybrid polymeric composites during CO_2-pulsed laser-cutting using RSM. *Lasers in Manufacturing and Materials Processing*, Vol. 8, 2021, pp. 157–182.

[50] Singh, H., J. Singh, S. Sharma, S. P. Dwivedi, and A. J. Obaid. Comparative performance of copper, graphite, brass and aluminium/graphite based different tool electrodes for optimizing the material removal rate during die-sinking EDM of stir-casted Al6061/SiC MMCs for sustainable manufacturing and energy applications. *Journal of Green Engineering*, Vol. 11, No. 1, 2021, pp. 922–938.

[51] Dwivedi, S. P., A. Saxena, S. Sharma, G. Singh, J. Singh, M. Mia, et al. Effect of ball-milling process parameters on mechanical properties of Al/Al_2O_3/collagen powder composite using statistical approach. *Journal of Materials Research and Technology*, Vol. 15, 2021, pp. 2918–2932.

[52] Jha, K., Y. K. Tyagi, R. Kumar, S. Sharma, M. R. M. Huzaifah, C. Li, et al. Assessment of dimensional stability, biodegradability, and fracture energy of bio-composites reinforced with novel pine cone. *Polymers*, Vol. 13, No. 19, 2021, id. 3260.

[53] Khare, J. M., S. Dahiya, B. Gangil, L. Ranakoti, S. Sharma, M. R. M. Huzaifah, et al. Comparative analysis of erosive wear behaviour of epoxy, polyester and vinyl esters based thermosetting polymer composites for human prosthetic applications using Taguchi design. *Polymers*, Vol. 13, No. 20, 2021, id. 3607.

[54] Dwivedi, S. P., N. Maurya, and S. Sharma. Study of CCLW, alumina and the mixture of alumina and CCLW reinforced aluminum based composite material with and without mechanical alloying. *Journal of the Institution of Engineers (India): Series D*, Vol. 103, 2022, pp. 319–331.

[55] Dwivedi, S. P., R. Sahu, A. Saxena, V. K. Dwivedi, K. Srinivas, and S. Sharma. Recovery of Cr from chrome-containing leather waste and its utilization as reinforcement along with waste spent alumina catalyst and grinding sludge in AA5052-based metal matrix composites. *Part E: Journal of Process Mechanical Engineering*, Vol. 236, 2021, pp. 160–170.

[56] Dwivedi, S. P., A. Saxena, and S. Sharma. Synthesis and characterization of spent alumina catalyst and grinding sludge reinforced aluminium based composite material. *Part C: Journal of Mechanical Engineering Science*, Vol. 236, 2021, pp. 5523–5534.
[57] Dwivedi, S. P., P. Pachauri, M. Maurya, A. Saxena, R. Butola, R. Sahu, et al. Alumina catalyst waste utilization for aluminum-based composites using the friction stir process. *Materials Testing*, Vol. 64, 2022, pp. 5533–5540.
[58] Rajawat, A. S., S. Singh, B. Gangil, L. Ranakoti, S. Sharma, M. R. M. Asyraf, et al. Effect of marble dust on the mechanical, morphological, and wear performance of basalt fibre-reinforced epoxy composites for structural applications. *Polymers*, Vol. 14, 2022, pp. 1325–1325.
[59] Chandel, P. S., Y. K. Tyagi, K. Jha, R. Kumar, S. Sharma, J. Singh, et al. Study of mode II interlaminar fracture toughness of laminated composites of glass and jute fibres in Epoxy for structural applications. *Functional Composites and Structures*, Vol. 3, 2021, pp. 44002–44002.
[60] Yeswanth, I. V., K. Jha, S. Bhowmik, R. Kumar, S. Sharma, and A. I. Rushdan. Recent developments in RAM based MWCNT composite materials: A short review. *Functional Composites and Structures*, Vol. 4, 2022, id. 024001.
[61] Virk, G. S., B. Singh, Y. Singh, S. Sharma, R. A. Ilyas, and V. Patyal. Abrasive water jet machining of coir fiber reinforced epoxy composites: A review. *Functional Composites and Structures*, Vol. 4, 2022, id. 014001.
[62] Juneja, S., J. S. Chohan, R. Kumar, S. Sharma, R. A. Ilyas, M. R. M. Asyraf, et al. Impact of process variables of acetone vapor jet drilling on surface roughness and circularity of 3D-printed ABS Parts: Fabrication and studies on thermal, morphological, and chemical characterizations. *Polymers*, Vol. 14, 2022, pp. 1367–1367.
[63] Khare, J. M., S. Dahiya, B. Gangil, L. Ranakoti, S. Sharma, M. Huzaifah, et al. Comparative analysis of erosive wear behaviour of epoxy, polyester and vinyl esters based thermosetting polymer composites for human prosthetic applications using Taguchi design. *Polymers*, Vol. 13, 2021, pp. 3607–3607.
[64] Dwivedi, S. P., M. Maurya, A. Saxena, and S. Sharma. Synthesis and characterization of spent alumina catalyst and grinding sludge reinforced aluminium based composite material. *Part C: Journal of Mechanical Engineering Science*, Vol. 236, 2021, pp. 5523–5534.
[65] Chandla, N. K., C. S. Jawalkar, and N. M. Suri. Effect of different weight percentage on mechanical properties of Aluminum metal matrix composites through hybrid reinforcement – A review. *International Journal for Scientific Research & Development*, Vol. 5, No. 5, 2017, pp. 91–96.
[66] Saheb D. A. Aluminum silicon carbide and aluminum graphite particulate composites. *ARPN Journal of Engineering and Applied Sciences*, Vol. 6, No. 10, 2011, pp. 41–46.
[67] Sidhu, S. S., T. R. Ablyaz, P. S. Bains, K. R. Muratov, E. S. Shlykov, and V. V. Shiryaev. Parametric optimization of electric discharge machining of metal matrix composites using analytic hierarchy process. *Micromachines* (*MDPI*), Vol. 12, No. 11, 2021, id. 1289.
[68] Dwivedi, S. P. and S. Sharma. Synthesis and characterization of Cr, eggshell and grinding sludge reinforced aluminum based metal matrix composites: An ingenious experimental approach. *Green Materials* (*ICE Virtual*), 2021, id. 024001.
[69] Ilyas, R. A., H. A. Aisyah, A. H. Nordin, N. Ngadi, M. Zuhri, M. Asyraf, et al. Natural-fiber-reinforced chitosan, chitosan blends and their nanocomposites for various advanced applications. *Polymers*, Vol. 14, 2022, pp. 874–874.
[70] Asyraf, M. R., A. Syamsir, N. M. Zahari, A. B. Supian, M. R. Ishak, S. M. Sapuan, et al. Product development of natural fibre-composites for various applications: Design for sustainability. *Polymers*, Vol. 14, 2022, pp. 920–920.
[71] Chohan, J. S., N. Mittal, R. Kumar, S. Singh, S. Sharma, J. Singh, et al. Mechanical strength enhancement of 3D printed acrylonitrile butadiene styrene polymer components using neural network optimization algorithm. *Polymers*, Vol. 12, 2020, pp. 2250–2250.
[72] Sharma, S., J. Singh, H. Kumar, A. Sharma, V. Aggarwal, A. S. Gill, et al. Utilization of rapid prototyping technology for the fabrication of an orthopedic shoe inserts for foot pain reprieve using thermo-softening viscoelastic polymers: a novel experimental approach. *Measurement and Control*, Vol. 53, 2020, pp. 519–530.
[73] Singh, Y., J. Singh, S. Sharma, A. Sharma, and J. S. Chohan. Process parameter optimization in laser cutting of coir fiber reinforced epoxy composite-a review. *Materials Today: Proceedings*, 2021, pp. 4738–4744.
[74] Chohan, J. S., R. Kumar, and T. B. Singh. Taguchi S/N and TOPSIS based optimization of fused deposition modelling and vapor finishing process for manufacturing of ABS plastic parts. *Materials*, Vol. 13, 2020, pp. 5176–5176.
[75] Prabhakaran, S., V. Krishnaraj, S. Sharma, M. Senthilkumar, R. Jegathishkumar, and R. Zitoune. Experimental study on thermal and morphological analyses of green composite sandwich made of flax and agglomerated cork. *Journal of Thermal Analysis and Calorimetry*, Vol. 139, 2020, pp. 3003–3012.
[76] Suriani, M. J., R. A. Ilyas, and M. Y. M. Zuhri. Critical review of natural fiber reinforced hybrid composites: processing, properties, applications and cost. *Polymers*, Vol. 13, 2021, pp. 3514–3514.
[77] Kumar, R., N. Ranjan, and V. Kumar. Characterization of friction stir-welded polylactic acid/aluminum composite primed through fused filament fabrication. *Journal of Materials Engineering and Performance*, Vol. 31, No. 3, 2021, pp. 2391–409.
[78] Ilyas, R. A., M. Zuhri, M. Norrrahim, M. Misenan, M. A. Jenol, S. A. Samsudin, et al. Natural fiber-reinforced polycaprolactone green and hybrid biocomposites for various advanced applications. *Polymers*, Vol. 14, 2022, pp. 182–182.
[79] Azlin, M., R. A. Ilyas, M. Zuhri, S. M. Sapuan, M. M. Harussani, S. Sharma, et al. 3D printing and shaping polymers, composites, and nanocomposites: A review. *Polymers*, Vol. 14, 2022, pp. 180–180.
[80] Muni, R. N., J. Singh, V. Kumar, S. Sharma, P. Sudhakara, V. Aggarwal, et al. Multiobjective optimization of EDM parameters for rice husk Ash/Cu/Mg-reinforced hybrid Al-0.7Fe-0.6Si-0.375Cr-0.25Zn metal matrix nanocomposites for

engineering applications: Fabrication and morphological analysis. *Journal of Nanomaterials*, Vol. 2022, 2022, id. 2188705.

[81] Ilyas, R. A., M. Y. M. Zuhri, H. A. Aisyah, M. R. M. Asyraf, S. A. Hassan, E. S. Zainudin, et al. Natural fiber-reinforced polylactic acid, polylactic acid blends and their composites for advanced applications. *Polymers*, Vol. 14, 2022, pp. 202–202.

[82] Sharma, S., V. Patyal, P. Sudhakara, J. Singh, M. Petru, and R. Ilyas. Mechanical, morphological, and fracture-deformation behavior of MWCNTs reinforced (Al-Cu-Mg-T351) alloy cast nanocomposites fabricated by optimized Mechanical milling and Powder metallurgy techniques. *Nanotechnology Reviews*, Vol. 11, 2022, pp. 65–85.

[83] Sharma, S., P. Sudhakara, M. Petru, J. Singh, and S. Rajkumar. Effect of nanoadditives on the novel leather fiber/recycled poly(ethylene-vinyl-acetate) polymer composites for multifunctional applications: Fabrication, characterizations, and multiobjective optimization using central composite design. *Nanotechnology Reviews*, Vol. 11, 2022, pp. 2366–2432.

[84] Singh, M., S. Sharma, A. Muniappan, D. Y. Pimenov, S. Wojciechowski, K. Jha, et al. In situ micro-observation of surface roughness and fracture mechanism in metal microforming of thin copper sheets with newly developed compact testing apparatus. *Materials*, Vol. 15, No. 4, 2022, id. 1368.

[85] Tiwari, A., S. Singh, R. Kumar, J. S. Chohan, S. Sharma, J. Singh, et al. The behavior residual properties of a sustainable concrete based composite material containing marble dust and foundry sand under elevated temperature. *Materials* (*MDPI*), Vol. 15, 2022, id. 3632.

[86] Prabhakaran, S., S. Sharma, A. Verma, S. M. Rangappa, S. Siengchin. Thermal and acoustical studies on natural alternative material for partition walls: A novel experimental investigation. *Polymer Composites* (*Wiley*), Vol. 43, 2022, id. 4711.

[87] Gill, A. S., S. Kumar, J. Singh, V. Aggarwal, and S. Sharma. A review of recent methods for tool wear reduction in electrical discharge machining. *Surface Review and Letters* (*SRL*)-*World Scientific Publishers*, Vol. 27, No. 12, 2020, id. 2030002.

[88] Jha, K., P. Tamrakar, R. Kumar, S. Sharma, J. Singh, R. A. Ilyas, et al. Effect of hybridization on physio-mechanical behavior of Vetiver and Jute fibres reinforced epoxy composites for structural applications: Studies on fabrication, physicomechanical, water-absorption, and morphological properties. *Journal of Industrial Textiles* (*SAGE*), Vol. 51, 2022, pp. 2642S–2664S.

[89] Alaneme, K. K. and K. O. Sanusi. Microstructural characteristics, mechanical and wear behaviour of aluminium matrix hybrid composites reinforced with alumina, rice husk ash and graphite. *Engineering Science and Technology, an International Journal*, Vol. 18, No. 3, 2015, pp. 416–422.

[90] Shaikh, M. B., T. Aziz, S. Arif, A. H. Ansari, P. G. Karagiannidis, and M. Uddin. Effect of sintering techniques on microstructural, mechanical and tribological properties of Al-SiC composites. *Surfaces and Interfaces*, Vol. 20, 2020, id. 100598.

[91] Umasankar, V., M. A. Xavior, and S. Karthikeyan. Experimental evaluation of the influence of processing parameters on the mechanical properties of SiC particle reinforced AA6061 aluminium alloy matrix composite by powder processing. *Journal of Alloys and Compounds*, Vol. 582, 2014, pp. 380–386.

[92] Arif, S., M. T. Alam, A. H. Ansari, M. B. Shaikh, and M. A. Siddiqui. Analysis of tribological behaviour of zirconia reinforced Al-SiC hybrid composites using statistical and artificial neural network technique. *Materials Research Express*, Vol. 5, 2018, id. 056506.

[93] Khajuria, A., R. Bedi, B. Singh, and M. Akhtar. EDM machinability and parametric optimisation of 2014Al/Al2O3 composite by RSM. *International Journal of Machining and Machinability of Materials*, Vol. 20, 2018, id. 536.

[94] Khajuria, A., M. Akhtar, and R. Bedi. A novel approach to envisage effects of boron in P91 steels through Gleeble Weld-HAZ simulation and impression-creep. *The Journal of Strain Analysis for Engineering Design*, Vol. 57, No. 8, 2021, pp. 647–663.

[95] Khajuria, A., M. Akhtar, M. K. Pandey, M. P. Singh, A. Raina, R. Bedi, et al. Influence of ceramic Al_2O_3 particulates on performance measures and surface characteristics during sinker EDM of stir cast AMMCs. *World Journal of Engineering*, Vol. 16, 2019, pp. 526–538.

[96] Han, M. C., S. Z. Cai, J. Wang, and H. W. He. Single-side superhydrophobicity in Si_3N_4-doped and SiO_2-treated polypropylene nonwoven webs with antibacterial activity. *Polymers*, Vol. 14, No. 14, 2022, id. 2952.

[97] Lv, B., S. Wang, T. Xu, and F. Guo. Effects of minor Nd and Er additions on the precipitation evolution and dynamic recrystallization behavior of Mg–6.0Zn–0.5Mn alloy. *Journal of Magnesium and Alloys*, Vol. 9, No. 3, 2021, pp. 840–852.

[98] Zhu, H. and R. Zhao. Isolated Ni atoms induced edge stabilities and equilibrium shapes of CVD-prepared hexagonal boron nitride on Ni (111) surface. *New Journal of Chemistry*, Vol. 46, 2022, pp. 17496–17504.

[99] Ye, R., P. Liu, K. Shi, and B. Yan. State damping control: A novel simple method of rotor UAV with high performance. *IEEE Access*, Vol. 8, 2020, pp. 214346–214357.

[100] Li, X., X. Yang, D. Yi, B. Liu, J. Zhu, J. Li, et al. Effects of NbC content on microstructural evolution and mechanical properties of laser cladded $Fe_{50}Mn_{30}Co_{10}Cr_{10}$-xNbC composite coatings. *Intermetallics*, Vol. 138, 2021, id. 138.

[101] Liu, J., S. MAO, S. Song, L. Huang, L. A. Belfiore, and J. Tang. Towards applicable photoacoustic micro-fluidic pumps: Tunable excitation wavelength and improved stability by fabrication of Ag-Au alloying nanoparticles. *Journal of Alloys and Compounds*, Vol. 884, 2021, id. 884.

[102] Liang, L., M. Xu, Y. Chen, T. Zhang, W. Tong, H. Liu, et al. Effect of welding thermal treatment on the microstructure and mechanical properties of nickel-based superalloy fabricated by selective laser melting. *Materials Science and Engineering A, Structural Materials: Properties, Microstructure and Processing*, Vol. 819, 2021, id. 141507.

[103] Zhong, Y., J. Xie, Y. Chen, L. Yin, P. He, and W. Lu. Microstructure and mechanical properties of micro laser welding NiTiNb/Ti6Al4V dissimilar alloys lap joints with nickel interlayer. *Materials Letters*, Vol. 306, 2022, id. 130896.

[104] Huang, Z., P. Luo, H. Zheng, and Z. Lyu. Sulfur-doped graphene promoted $Li_4Ti_5O_{12}$@C nanocrystals for lithium-ion batteries. *Journal of Alloys and Compounds*, Vol. 908, No. 5, 2022, id. 164599.

[105] Luo, Y., Y. Xie, W. Geng, J. Chu, H. Wu, D. Xie, et al. Boosting fire safety and mechanical performance of thermoplastic polyurethane by the face-to-face two-dimensional phosphorene/MXene architecture. *Journal of Materials Science and Technology*, Vol. 129, 2022, pp. 27–39.

[106] Gong P., D. Wang, C. Zhang, Y. Wang, Z. Jamili-Shirvan, K. Yao, et al. Corrosion behavior of TiZrHfBeCu(Ni) high-entropy bulk metallic glasses in 3.5wt% NaCl. *npj Materials Degradation*, Vol. 6, 2022, id. 77.